
Article:
Lessing, S, Dobson, DP, Rost, S et al. (2022) Kinetic effects on the 660 km-phase transition in mantle upstreams and seismological implications. Geophysical Journal International, 231 (2). pp. 877-893. ISSN: 0956-540X

https://doi.org/10.1093/gji/ggac196

Kinetic effects on the 660 km-phase transition in mantle upstreams and seismological implications.

Stephan Lessing[1,5,*], David P. Dobson[2], Sebastian Rost[3], Laura Cobden[1,4], Christine Thomas[1]

[1]Institute of Geophysics, Westfälische Wilhelms-Universität Münster, Corrensstraße 24, 48149 Münster, Germany
[2]Department of Earth Sciences, University College London, Gower Street, London WC1E 6BT, United Kingdom
[3]School of Earth and Environment, Institute of Geophysics and Tectonics, University of Leeds, Leeds LS2 9JT, United Kingdom
[4]Department of Earth Sciences, Utrecht University, Princetonlaan 8a, 3584CB Utrecht, The Netherlands
[5]Now at: Ferchau GmbH, Branch Office Bremen-City, Lloydstraße 4/6, 28217 Bremen, Germany

Accepted *May 19, 2022*. Received *May 16, 2022.* In original form *February 5, 2022.*

*Corresponding author:
Stephan Lessing
Thomastraße 7
27753 Delmenhorst
Germany
E-mail: stephan.lessing@gmail.com
Tel. +49 (0) 42 21 12 31 472

Abstract

The effects of reaction kinetics of bridgmanite and ferropericlase transforming to ringwoodite on elastic properties in upwelling mantle are investigated using data of kinetic experiments and internally self-consistent thermodynamic modelling of density and seismic velocities. The kinetic experiments show inhibited grain growth of ringwoodite. At the initiation of ringwoodite growth, bridgmanite completely transforms to a metastable pyrope-bearing garnet. Ringwoodite then gradually grows from the metastable assemblage of ferropericlase and garnet. The changes in mineralogy result in a low-velocity zone directly above the 660 km seismic discontinuity due to the lower seismic velocities and densities of ferropericlase and garnet compared to ringwoodite and bridgmanite. The modelling of the effects of reaction kinetics and its effect on seismic structure at ~660 km depth shows more sensitivity to grain size than to temperature and upwelling rate. Modelling 1-D synthetic seismograms of PP (SS) underside reflections off the kinetically inhibited backward reaction to ringwoodite shows advanced travel times of underside reflections off ~660 km depth of 0.2 - 0.8 s (1.2 - 1.6 s) for upwelling rates of 50 cm/yr and initial grain sizes between 5 and 20 cm due to the low-velocity zone above the 660 km discontinuity. The finite width of the low-velocity layer results in frequency-dependent behaviour of PP and SS underside reflection amplitudes, with higher amplitudes towards shorter periods. The effect on the travel times of P-to-s conversions used for receiver function is small (< 0.7 s) but the inhibited backward reaction leads to strong amplitude changes and significant waveform variations. The effects of reaction kinetics in mantle upwellings might serve as an additional means to map regions of large-scale upwellings and to constrain grain size in the lower mantle.

Key words: Phase transitions, Composition and structure of the mantle, High-pressure behaviour, Body waves

1 Introduction

The seismic structure of the Earth's mantle transition zone between upper and lower mantle is dominated by two seismic discontinuities at which the seismic velocities and density increase over short depth intervals. These discontinuities are found in most spherically averaged 1-D Earth reference models, e.g., ak135 (Kennett et al., 1995), and are considered as the seismic expressions of solid-solid phase transitions and mineral reactions (both hereafter called phase transformations) of the olivine system (e.g., Ringwood, 1969; Helffrich, 2000; Shearer, 2000; Weidner & Wang, 2000; Deuss, 2015). Thermodynamic calculations of mantle mineral phase relations are frequently used to interpret observations of seismic velocities and seismic discontinuity structure and help to identify and quantify their thermal and compositional origins (e.g., Cobden et al., 2008; Ritsema et al., 2009; Saki et al., 2019; Vilella et al., 2021; Waszek et al., 2021).

For thermodynamic modelling of phase equilibria and their seismic properties, the Earth's mantle is usually assumed as vigorously convecting, homogeneous and well mixed. However, geodynamic studies have demonstrated the long-term existence of thermal and compositional heterogeneities throughout the mantle (e.g., Allègre & Turcotte, 1986; Kellogg et al., 2002; Tackley et al., 2005; Ballmer et al., 2017). Small diffusivities of the solid mantle (e.g., Hofmann & Hart, 1978; Farber et al., 1994) lead to the question: to what degree have the mineral assemblages reached thermodynamic equilibrium and mineral transformations been completed? The mechanisms of mineral transformations, i.e., their reaction kinetics, might therefore affect the dynamics and seismic structure of the Earth's mantle (e.g., Kubo et al., 2002; Kubo et al., 2008). Therefore, taking the reaction kinetics into account might be essential for our interpretation of the seismic signals in terms of mantle composition and temperature.

The influence of reaction kinetics on mineral transformations was first investigated in detail when seismologists looked for mechanisms of deep earthquakes in subducting slabs (e.g., Sung & Burns, 1976; see Kirby, 1996, for a review). Motivated by observations of apparently stagnant slabs at ~660 km depth in seismic tomography models (e.g., van der Hilst, 1991; Fukao et al., 2001; Fukao et al., 2009), Kubo et al. (2002) and Kubo et al. (2008) investigated the reaction kinetics of phase transformations of ringwoodite to ferropericlase and bridgmanite and of garnet to bridgmanite at ~660 km depth and temperature conditions typical for subducting slabs. The kinetic experiments by Kubo et al. (2002) and Kubo et al. (2008) show that low temperatures within the slab decrease the mobility of atoms in the crystal lattice and hence

could reduce reaction rates of mineral transformations. The kinetic inhibition of the phase transformations of ringwoodite to ferropericlase and bridgmanite and of garnet to bridgmanite result in neutral to positive buoyancy which may lead to stagnant slabs. Recently it has also been shown that kinetics of the bridgmanite to post-perovskite phase transition can affect visibility of the D" reflector (Langrand et al., 2019).

Reaction mechanisms of mineral transformations can also change for higher temperatures. Studies by Gasparik (1996a), Gasparik (1996b), Weidner & Wang (1998), Irifune et al. (1998) and Hirose (2002) show that the reaction mechanism of ringwoodite to ferropericlase and bridgmanite changes for mantle temperatures larger than 2100 K. This temperature is considered as a reasonable estimate for the centre of hot mantle upwellings (e.g., Sleep, 1990; Schilling, 1991; Weidner & Wang, 1998). For aluminium contents of approximately 5 wt% and temperatures of at least 2100 K, ringwoodite transforms to bridgmanite and ferropericlase via the dissociation of ringwoodite to ferropericlase and majorite garnet, and finally to ferropericlase and bridgmanite (Gasparik, 1996a; Gasparik, 1996b; Weidner & Wang, 1998; Irifune et al., 1998; Hirose, 2002).

Kinetic studies by Shimojuku et al. (2014) and Dobson & Mariani (2014) have investigated the reaction kinetics for the reverse reaction of bridgmanite and ferropericlase to ringwoodite in upwelling mantle. The kinetic experiments show that the growth of ringwoodite is kinetically inhibited, and that bridgmanite transforms to pyrope-bearing garnet. The reverse reaction from bridgmanite and ferropericlase to ringwoodite and garnet (in mantle upwellings) requires diffusion on a much larger length-scale than the forward reaction because macroscopic grains of bridgmanite and ferropericlase must recombine to form ringwoodite (Dobson & Mariani, 2014). In the case of aluminous garnets, the interface between ringwoodite and garnet develops a fingering instability resulting in a complex intergrowth (Figure 1). Garnet incorporates the aluminium oxide of the bridgmanite into its crystal lattice and has the same bulk chemistry as the bridgmanite before the transformation, and hence this isochemical transformation is fast compared to the diffusion-controlled reaction between bridgmanite and ferropericlase. Over time, this chemically metastable garnet reacts with ferropericlase, and the stable phase, ringwoodite, starts to nucleate and grow at the interface between ferropericlase and garnet.

The growth of ringwoodite on the ferropericlase grains is most likely controlled by the slow diffusion of SiO_2 from garnet across the reaction layer into the grains of ferropericlase. The ringwoodite growth rate is sensitive to the initial grain size of lower mantle minerals (Dobson

& Mariani, 2014). The initial ferropericlase grain size is the typical length scale of diffusion. The amount of ringwoodite formed depends on bulk composition and ambient temperature. The bulk composition affects the individual molar amounts of the mineral solid solutions. The ambient mantle temperature influences the equilibrium phase relations and mobility of atoms, determining the diffusion rate of atoms across interfaces and grain boundaries (e.g., Putnis, 1992). The initial grain size controls the relative proportions of reactants and products for a given amount of diffusion across the reacting interface.

Our study investigates the effects of reaction kinetics for the recombination of bridgmanite and ferropericlase to ringwoodite in mantle upwellings on density and seismic wave velocities to assess the possibility to observe the effects of the kinematically inhibited back reaction seismically. The kinetically inhibited growth of ringwoodite is determined for a range of mantle temperatures at 660 km depth, varying grain sizes and mantle upwelling rates. The changed volume fractions of the minerals as a function of pressure are used to calculate profiles of density, P- and S-wave velocities for kinetically inhibited and equilibrated phase assemblages using internally self-consistent thermodynamic modelling. These models are used to compute 1-D synthetic seismograms for PP and SS underside reflections off the resulting discontinuity and for P-to-s conversions at the discontinuity (known as P receiver functions), two probes often used to study upper mantle discontinuities, to assess the effects on travel times and waveforms. Our aim is not to carry out a seismic study at this point to search for such effects in observed seismic data. This work presents a previously unstudied effect of mantle phase transitions on seismic data that should be kept in mind in future seismic studies.

2 Methods

The kinetically inhibited growth of ringwoodite and its effects on phase assemblages and seismic properties are computed in five steps:

1. calculation of phase equilibria,
2. calculation of the thickness of the ringwoodite layer produced for a given temperature, grain size and mantle upwelling rate,
3. mass balancing consumption of metastable ferropericlase and garnet,
4. calculation of density and seismic wave velocities.
5. computation of 1-D synthetic seismograms

2.1 Calculation of phase equilibria

Phase equilibria for the CFMAS (calcium oxide, iron(II) oxide, magnesium oxide, aluminium oxide and silica) system are calculated for a pyrolitic mantle composition (Table 1) with the Perple_X program package (Connolly, 2005) that utilises the free-energy minimization algorithm by Ita & Stixrude (1992) and Stixrude & Lithgow-Bertelloni (2005), and the elastic and thermodynamic properties and the solid solution model of Stixrude & Lithgow-Bertelloni (2011). From the calculated phase equilibria, profiles of P-wave velocity, S-wave velocity and density are extracted along adiabatic mantle geotherms (e.g., Cobden et al., 2008). The values of P-wave velocity, S-wave velocity, and density of the phase assemblage at a specific P-T-point are calculated as the Hill average of Voigt and Reuss bounds of the constituent minerals (Voigt, 1928; Reuss, 1929; Hill, 1965).

2.2 Kinetically inhibited growth of ringwoodite and mineral reactions

The seismic structures of the kinetically inhibited phase assemblages are calculated from the grain growth of ringwoodite for fixed temperature, grain size and upwelling rate (Figure 2). Before we describe the calculations of kinetically inhibited growth of ringwoodite and its impact on seismic properties, we compare the mineral reactions at thermodynamic equilibrium with those observed by Dobson & Mariani (2014).

The recombination reaction at thermodynamic equilibrium is described as

$$MgO + MgSiO_3 \leftrightarrow Mg_2SiO_4 \quad (1)$$

ferropericlase + bridgmanite ↔ ringwoodite

Dobson & Mariani (2014) observe in the kinetic experiments that bridgmanite entirely transforms to garnet, where the aluminium-bearing bridgmanite transform to pyrope garnet:

$$3.75\ MgSiO_3 \cdot 0.25\ Al_2O_3 \leftrightarrow 0.75\ Mg_4Si_4O_{12} + 0.25\ Mg_3Al_2Si_3O_{12} \quad (2)$$

aluminous bridgmanite ↔ majorite garnet + pyrope garnet

The consumption of bridgmanite to ringwoodite comprises of several reactions. At the onset of ringwoodite growth, the entire amount of bridgmanite transforms to garnet,

$$MgSiO_3 \rightarrow 0.25\ Mg_4Si_4O_{12}, \quad (3)$$

bridgmanite → majorite garnet

creating an excess of garnet compared to conditions at thermodynamic equilibrium. The difference between the decrease of ferropericlase with kinetic inhibition effects and the phase fraction of ferropericlase is later used to infer the decrease of garnet which recombines with ferropericlase to give ringwoodite via the reaction

$$MgO + 0.25\ Mg_4Si_4O_{12} \leftrightarrow Mg_2SiO_4 \quad (4)$$

ferropericlase + majorite garnet ↔ ringwoodite

The kinetically inhibited growth of ringwoodite and the dependent mineral transformations of bridgmanite and garnet are assumed to leave calcium-bearing garnets and the exsolution of calcium perovskite unaffected. Therefore, amounts of calcium-bearing garnets and calcium perovskite are extracted from the thermodynamic calculations.

We now derive how we calculate the growth kinetics of ringwoodite and account for the mineral reactions mentioned above. The growth kinetics of ringwoodite are controlled by two parameters which are determined in experiments: its enthalpy ΔH_a and its reaction rate constant k_0 which is closely linked to the reaction entropy ΔS_a.

For a mineral transformation from mineral assemblages A and B to a mineral assemblage C, the reaction rate is proportional to the molar concentrations of mineral phases A and B, C_A and C_B (Putnis, 1992):

$$\text{Reaction rate} \propto K^* C_A C_B \quad (5)$$

In our case, C_A and C_B are the concentration of ferropericlase and majorite garnet. The equilibrium constant of the reaction K^* is a function of the change of reaction Gibbs free energy, ΔG_a,

$$K^* = exp(-\Delta G_a/(R\ T)\ ) = exp(\Delta S_a/R)\ exp(-\Delta H_a/(R\ T)\ ) \quad (6)$$

using the definition of the reaction Gibbs free energy $\Delta G_a = \Delta H_a - T\Delta S_a$ with the enthalpy of the reaction ΔH_a and the entropy of the reaction ΔS_a. R denotes the gas constant and T is temperature. The reaction rate can be rewritten as

$$\text{Reaction rate} = c\ exp(\Delta S_a/R)\ exp(-\Delta H_a/(R\ T))\ C_A\ C_B \quad (7)$$

where c is a constant. As the concentration of the reactants changes during the reaction, the reaction rate will change accordingly. The reaction rate thus becomes a function of the phase fraction C

$$\text{Reaction rate} = k\ f(C) \quad (8)$$

where the reaction rate parameter k describes how the reaction rate depends on the concentration of the reactants. Therefore, the rate constant is

$$k = k(T) = c\ exp(\Delta S_a/R)\ exp(-\Delta H_a/(R\ T)\ ) = k_0\ exp(-\Delta H_a/(R\ T)\ ) \quad (9)$$

with the reaction rate constant $k_0 = c\ exp(\Delta S_a/R)$ where c is an experimentally determined factor.

Dobson & Mariani (2014) show that the growth kinetics of ringwoodite are controlled by diffusion kinetics. In this case, the rate of growth of the interface is linear with the square-root of time and the thickness of reaction rims measured at each temperature can be converted into apparent rate constants (Watson & Price, 2002). Following Tammann (1920) and Watson & Price (2002), the temperature dependent rate constant $k(T)$ is given by

$$k(T) = \frac{1}{2}\frac{\mathrm{d}}{\mathrm{d}t}x^2 \quad (10)$$

where x is the thickness of the growing interface and t is time. Integration of (10) gives the interface thickness evolution as a function of time and temperature:

$$x(t, T) = ((2\ k(T)\ t)^{1/2}). \quad (11)$$

To model the kinetic inhibition of ringwoodite growth, the interface grows until reaching the assumed initial grain size d. In this study, radially isotropic growth of the ringwoodite interface

is assumed. We therefore normalise the ringwoodite interface thickness evolution (11) with half of the desired grain size (d) which results in a relative grain size: :

$$x_{rel}(t, T) = ((2\ k(T)\ t)^{1/2})/(0.5\ d). \quad (12)$$

Since temperatures are approximately constant along the chosen adiabats, we assume a constant temperature T_0 during the reaction:

$$x_{rel}(t) = ((2\ k(T_0)\ t)^{1/2})/(0.5\ d). \quad (13)$$

Due to its inverse dependency on grain size d, eq. (13) indicates that growth of ringwoodite takes more time in case of large grain size.

Assuming an upwelling rate v and utilizing the depth-to-pressure scale used by Cobden et al. (2008), the time of grain growth is converted to a grain growth curve as a function of pressure, $x_{rel}(P)$. In our calculations, upwelling rates in the mantle are estimated to range between 1 and 100 cm/yr considering current heat flux estimates in upwelling mantle (e.g., Sleep, 1990; Courtillot et al., 2003) and geodynamic modelling experiments (Farnetani & Hofmann, 2010). The average grain size in the lower mantle is estimated to range between 1 µm (Yamazaki et al., 1996) and 10 cm (Solomatov, 1996; Korenaga, 2005) based on varying estimates of grain growth kinetics of mineral transformations in downwelling, or primordial, mantle. In the interior of a subducting slab, Yamazaki et al. (1996) and Yamazaki et al. (2005) find very slow grain growth rates for ferropericlase and bridgmanite, with grain sizes ranging between 10 µm to 100 µm for temperatures typical for subduction zones and for 10 million years after grain nucleation, but Fei et al. (2021) find a much smaller grain size exponent compared to Yamazaki et al. (1996). Their estimate for grain size in subducted slabs is on the order of 30-45 µm. Solomatov et al. (2002) question estimates of grain size for the bulk mantle as they cannot be reconciled with viscosity models or laboratory data for other materials. Solomatov et al. (2002) argue that the experiments have not been run sufficiently long to evaluate grain growth kinetics beyond transient effects. Solomatov (1996) and Korenaga (2005) have additionally suggested that deep-mantle plumes might have a significantly larger grain size than the ambient lower mantle due to (i) the temperature of the source region of the mantle upwelling, (ii) the kinetics of grain growth from an early magma ocean, and (iii) seismic tomographic imaging of wide slow structures which have been interpreted as wide plume roots (French & Romanowicz, 2015).

2.3 Mass balancing consumption of metastable ferropericlase and garnet

We follow the workflow in Figure 2 to calculate volume fractions of the mineral phases affected by the kinetically inhibited growth of ringwoodite for given grain size d, upwelling rate v and constant temperature T_0. Ringwoodite starts to grow at pressure P_{Start} where the molar amount of ringwoodite is non-zero in the equilibrium phase assemblage. The kinetically inhibited growth of ringwoodite is calculated as the convolution of the grain growth curve and the derivative of the molar amounts of ringwoodite at thermodynamic equilibrium as a function of depth. The growth curve x_{rel} is truncated where the relative growth of ringwoodite equals 1. At this pressure, hereafter called P_{end}, the molar amount of ringwoodite with kinetically inhibited growth conditions is considered to be equal to the amount of ringwoodite at thermodynamic equilibrium. Using the molar amount of ringwoodite at P_{end}, $n_{\text{Rw,end}}$, we convert the grain growth curve (12) into molar amount of ringwoodite:

$$n_{\text{Rw}}(P) = n_{\text{Rw,end}}\, x_{\text{rel}}(P) \tag{13}$$

We calculate the mass balances of ferropericlase, majorite garnet and pyrope garnet, following the mineral reactions in (2) – (4). Using molar volumes of the individual mineral phases from our thermodynamic calculations in section 2.1, we convert molar amounts to volume fractions within the pressure interval from P_{end} to P_{start}.

2.4 Calculation of density and seismic wave velocities

Utilizing their volume fractions calculated as described in section 2.3, we calculate the seismic properties of the kinetically inhibited phase assemblages, for the Hill average of Voigt and Reuss bounds of the constituent minerals (Voigt, 1928; Reuss, 1929; Hill, 1965). For each mineral, the density and seismic velocity are determined at the given pressure and temperature. The seismic properties of the kinetically inhibited phase assemblages are fit to the seismic profiles of phase assemblages at thermodynamic equilibrium for the corresponding adiabatic mantle geotherm.

2.5 Computation of 1-D synthetic seismograms

The mineral physical results can be used to test if the effects of the kinetically inhibited

transformation of bridgmanite and ferropericlase to ringwoodite can be observed in seismological data. We focus on effects of PP and SS underside reflections and P-to-s conversions as they are commonly used probes to study upper mantle discontinuities. For this, the computed profiles of density, P wave and S wave velocity for equilibrated and kinetically inhibited phase assemblages are used to calculate 1-D reflectivity synthetic seismograms (Fuchs & Müller, 1971; Müller, 1985) for a range of dominant periods. Attenuation values are taken from PREM (Dziewonski & Anderson, 1981). For comparison, 1-D reflectivity synthetic seismograms using the 1-D velocity model ak135 (Kennett et al., 1995) and attenuation of PREM (Dziewonski & Anderson, 1981) are computed. Dominant periods of PP underside reflections are 1, 3, 5, 8 and 10 s. A source at 50 km depth is chosen and the data are analysed on the vertical component. For SS underside reflections, dominant periods are 5, 8, 10, 15 and 20 s. The source is at 50 km depth and the data are analysed on the transverse component. 21 receivers are distributed as a linear array around 120° epicentral distance with an aperture of 5°. An epicentral distance of 120° is within typical distances used for PP and SS precursor studies (e.g., Shearer, 1991; Thomas & Billen, 2009; Deuss, 2009). The seismograms are aligned on the PP/SS arrival and are normalised to unit amplitude.

For the P-to-s conversions we use dominant periods of 0.5 s, 1 s and 2 s with a source depth of 2 km to avoid interference of the P660s (and P410s for reference) arrivals with depth phases. We use a linear array with 1° receiver spacing between 40° and 80°. We calculate three-component seismograms (Z, R, T) but only analyse the radial component. Due to the simple source time function and the consistent waveforms, we abstain from deconvolving the vertical component P-wave and interpret the relevant waveform variation in the Results section.

3 Results

3.1 Effects of kinetic inhibition on seismic fine structure

The effects of kinetic inhibition on phase assemblages are compared with phase assemblages at thermodynamic equilibrium with regard to the mineral proportions and seismic properties. The kinetically inhibited growth of ringwoodite and the metastable assemblage of ferropericlase and pyrope-bearing garnet change the phase proportions above the onset depth of the phase transformation (Figure 3). For equilibrated phase assemblages at a temperature of ~1850 K (following the adiabat with 1300°C potential surface temperature, abbreviated hereafter as "1300°C adiabat"; please see Table 2 and Cobden et al., 2008 for details), ringwoodite

dissociates to ferropericlase and bridgmanite within a pressure interval of ~0.1-0.2 GPa (i.e., ~2 km) at ~23.4 GPa (i.e., at ~659 km depth) (Figure 3a). The amount of garnet decreases due to the exsolution of bridgmanite, starting at ~22.7 GPa (~642 km).

The thickness of inhibited growth of ringwoodite is sensitive to temperature, grain size and mantle upwelling rate. For 5 cm grain size and 50 cm/yr upwelling rate, the kinetic inhibition leads to a growth of ringwoodite over a pressure interval of 1 GPa (~25 km) (Figure 3b). The gradual growth of ringwoodite results in a gradual consumption of ferropericlase. At the pressure where ringwoodite starts to grow, the entire amount of bridgmanite reacts to garnet, thus its volume fraction increases to 70%. The recombination reaction of garnet and ferropericlase to ringwoodite gradually decreases the amount of garnet towards lower pressures.

The excess of garnet changes the seismic structure around 660 km depth (Figure 3c). Since garnet has lower P- and S-wave velocities (garnet: $v_p \approx 9.8$ km/s, $v_s \approx 5.2$ km/s at 23.4 GPa and 1850 K) than ringwoodite and bridgmanite (ringwoodite: $v_p \approx 10.2$ km/s, $v_s \approx 5.6$ km/s; bridgmanite: $v_p \approx 11.2$ km/s, $v_s \approx 6.3$ km/s at 23.4 GPa and 1850 K), the kinetically inhibited growth of ringwoodite and the abundance of garnet results in a low-velocity layer above the 660 km discontinuity of $\Delta v_p \approx -5\%$, $\Delta v_s \approx -7\%$ (Figure 45). The low-velocity layer above the lower boundary of the ringwoodite-forming reaction thus increases the P- and S-wave impedance contrast. When the growth of ringwoodite has reached equilibrium conditions, the profiles of density and seismic wave speeds intersect the profiles of the phase assemblages at thermodynamic equilibrium.

The effects of initial grain size d and mantle upwelling rate v can be described by a kinetic parameter D which is proportional to the upwelling rate and the squared grain size (Dobson & Mariani, 2014):

$$D \sim v\, d^2.$$

Scenarios of kinetic inhibition with different initial grain sizes and upwelling rates give the same results if they can be described by the same kinetic parameter. Therefore, the kinetic parameter is an appropriate entity to compare scenarios of kinetically inhibited phase assemblages. Since the kinetic parameter scales with the square of initial grain size d, the kinetic inhibition of ringwoodite is more sensitive to grain size than to upwelling rate. In this study, we

set the proportional factor to unity and use

$$D = v\, d^2.$$

in order to compare scenarios of initial grain size d and mantle upwelling rate v.

The thickness of the low-velocity layer, i.e., the depth interval between the onset and the completion of ringwoodite growth, increases exponentially with increasing kinetic parameter of the kinetic parameter (Figure 5). The exponential behaviour can be explained by the grain growth equation which includes the Arrhenius relation for the reaction rate parameter $k(T)$ (cf. Eq. (9)). For kinetic parameters D between 10 and 100 cm³/yr, kinetic inhibition occurs over a pressure interval of ~0.1 GPa which is as narrow as the transformation pressure interval of the recombination of ringwoodite from ferropericlase and bridgmanite. A transformation pressure interval of ~0.1 GPa is equivalent to a low-velocity layer of thickness ~2 km which is likely below the resolution threshold even of short period PP waves and at the resolution level for receiver function (Ps). Seismic waves therefore sample the reflector and low-velocity layer above in the same way as the reflector for phase assemblages at thermodynamic equilibrium. The onset of seismically detectable kinetic inhibition in terms of the kinetic parameter D is $D > 100$ cm³/yr for 1850 K, $D > 1000$ cm³/yr for 1960 K and $D > 2500$ cm³/yr for 2050 K. The temperature dependence can be explained by the increased diffusion of ions at higher temperatures.

3.2 Synthetic seismograms

We have calculated 1-D synthetic seismograms from the synthetic velocity and density profiles using the reflectivity methods (Fuchs & Müller, 1971; Müller, 1985) as described in section 2.4. Here we discuss the effects of the kinematically inhibited velocity structures on PP/SS underside reflections and P-to-s conversions, two probes regularly used for the study of upper mantle discontinuities.

3.2.1 PP and SS Precursors

The seismograms calculated for the velocity models with kinetically inhibited recombination reaction of ringwoodite from bridgmanite and ferropericlase are compared to seismograms for velocity models with equilibrated phase assemblages. Using linear vespagrams (Davies et al.,

1971; Muirhead et al., 1976), PP/SS and P660P/S660S waveforms are extracted for travel times predicted by ak135 (Kennett et al., 1995) (Figure 6).

For velocity models where the kinetic inhibition of the ringwoodite growth results in a thicker low-velocity layer of the order of ~25 km, the PP/SS precursors off the reflector caused by kinetically inhibited recombination of ringwoodite are noticeably advanced for reaction intervals wider than 25 km compared to PP/SS precursors reflected off discontinuities of equilibrated phase transformations (Figure 3b). The travel time advances also affect secondary phases of the underside reflections such as depth phases, e.g., pP660P (Figure 6). For the kinetic parameters tested here, the maximum travel time advances for PP underside reflections are ~0.8 s, whereas maximum travel time advances for SS underside reflections are ~1.3 s (Figure 7). These travel time residuals correspond to apparent maximum shifts of the discontinuity depth on the order of 5 km.

Amplitudes for PP precursors with a dominant period of 1 s reflected off the kinetically inhibited formation of ringwoodite vary between 120% and 160% relative to the equilibrium model at 1850 K. For the same temperature, amplitudes of SS precursors with a dominant period of 5 s range between 120% and 160% relative to the equilibrium model. The precursor amplitudes for the kinetically inhibited phase assemblages decrease with increasing periods (Figure 8). The transition from enhanced to apparently unaltered precursor amplitudes is at a dominant period of 5 s for PP and 10 s for SS. Moreover, the PP and SS precursor amplitudes increase with increasing kinetic parameters and increasing thickness of the low-velocity layer. The PP/SS precursors off the lower boundary of the phase transformation are less affected by interference with PP/SS precursors off the gradient above the low-velocity layer.

While it appears that underside reflections of PP waves at the ringwoodite to bridgmanite plus ferropericlase transition are more difficult to detect than the corresponding SS underside reflection (Estabrook & Kind, 1996), there is evidence for P660P waves in some regional studies (e.g., Deuss et al., 2006; Thomas & Billen, 2009; Schmerr & Thomas, 2011, Saki et al., 2014) and usually the amplitudes of observed P660P waves are smaller than predicted by PREM or a pyrolytic mantle. There is also a noted discrepancy between the detection of P660P and its equivalent underside reflection of PKPPKP (P'660P') (Day & Deuss, 2013). The scarcity of P660P detections in recorded data can likely be explained by compositional and thermal effects that are not captured in our modelling and the assumed pyrolytic starting model (Lessing et al., 2015; Guo & Zhou et al.,2020; Waszek er al., 2021).

Underside reflection of PP from the 660 km phase transition are rarely detected in recorded data although such detections exist (Deuss et al., 2006; Day & Deuss, 2013).

The finite width of the low-velocity layer (Figure 3a) and the vertical resolution of the seismic waves lead to a frequency-dependent behaviour of P660P/S660S precursor amplitudes (Figure 9). PP waves with 1 s dominant period appear to resolve the increased P wave impedance contrast off the reflector caused by the kinetically inhibited recombination of ringwoodite. The increased P wave impedance contrast results in increased PP precursor amplitudes compared to the reflections for equilibrated phase assemblages. If the dominant period is increased, PP precursor amplitudes off the reflector with kinetic inhibition decrease and have similar PP precursor amplitudes off the reflector as those without kinetic inhibition.

3.2.2 P-to-s conversions (P receiver functions)

Examples of the synthetic waveforms for the kinetically inhibited models and pyrolitic models at equilibrium conditions are shown in Figure 10. For varying temperatures at equilibrium, we observe strong conversions from the 660 km discontinuity and other discontinuities (e.g., 410-km as well as shallower) with minor waveform and amplitude variations. We calculated synthetics for dominant periods of 0.5 s, 1 s, and 2 s and observe very minor variability of the results. While absolute travel times for P- and P-coda arrivals vary, differential travel time variations are minor, with 0.2 s and 0.6 s for the 1960 K and 2050 K simulations, respectively, compared to the 1850 K simulations. Waveform variations are limited to larger moveout for a deeper transition, arriving 5.1 to 8.9 s after P660s.

For the kinetically inhibited transformations we observe strong waveform variations with temperature, where the waveforms of the high temperature models show a dominant precursor about 7 s preceding the arrival from P660s (Figure 10b and c). The precursor due to the low velocity zone will lead to a likely detectable negative polarity precursor in P-wave receiver functions (see Figure S1 for an additional velocity profile at 2050 K). Those detectable negative polarity precursors have been reported in some up-flowing regions of the mantle (e.g., Negi et al., 2022). We observe amplitude variations dependent on grain size, upwelling rate, and temperature (Figure 10d). Amplitudes vary between 52% and 122% relative to the equilibrium model at 1960 K with the smallest amplitudes observed for the highest temperatures. Interference effects lead to apparent inverted waveforms for the P-to-s conversion relative to P. Both amplitude and waveform variations for these models would be large enough to be

488 observed in receiver function analyses.
489
490 Travel times relative to P vary slightly for the different models. We observe travel time
491 variations of ±0.3 s relative to the equilibrium model at 1960 K. While detectable, these might
492 be difficult to detect for recorded data due to the 3-D velocity variations known to exist in upper
493 mantle.
494
495 **4 Discussion**
496
497 **4.1 Estimates of uncertainties**
498
499 The effects of initial grain size and upwelling rate on the seismic properties of kinetically
500 inhibited phase assemblages have been investigated in section 3.1. Among the kinetic input
501 parameters, i.e., kinetic rate parameter k_0, reaction enthalpy ΔH_a and temperature T),
502 uncertainties of the reaction enthalpy predominantly affect the seismic properties of kinetically
503 inhibited phase assemblages (Figure 11a and b). Dobson & Mariani (2014) measure the
504 enthalpy of the reaction with an uncertainty of ±40 kJ mol^{-1} for the ringwoodite layer (Table 1).
505 Varying the enthalpy of the reaction with this value while keeping remaining parameters
506 constant in eq. (9) results in variations of the growth time of ringwoodite until equilibrium
507 conditions by one order of magnitude (Figure 11b).
508
509 Converting growth time into the thickness of the reaction interval using the upwelling rate gives
510 uncertainties of the reaction interval of one order of magnitude. Given the uncertainty of the
511 enthalpy of the reaction for the ringwoodite layer, the reaction interval could therefore range
512 from 1 km to ~250 km for kinetic parameters ranging from 1 to 10.000 cm^3/yr. On the one hand,
513 reaction intervals with a width of 1-10 km are close to the vertical resolution of PP and SS
514 precursors (e.g., Thomas & Billen, 2009; Schmerr & Thomas, 2011) and it might be challenging
515 to discriminate kinetic effects from other influences on reaction intervals. On the other hand,
516 reaction intervals with widths of 100-200 km would give increased PP and SS precursor
517 amplitudes due to the increased P wave and S wave impedance contrast and due to the more
518 gradual change of seismic properties from the low-velocity region relative to seismic properties
519 at thermodynamic equilibrium. P-to-s conversions at the discontinuities beneath the receiver
520 typically show higher resolution and are likely able to detect even the thinner layers inferred
521 for the smaller kinetic parameters. Thicker reaction intervals would result in strongly reduced
522 amplitudes of Ps. Reaction intervals of 100-200 km would also affect phase transformations at

smaller pressures/shallower depths, e.g., the wadsleyite to ringwoodite transition, as well as the phase transformations from pyroxene to garnet and from garnet to calcium silicate perovskite. The kinetics of the olivine to wadsleyite phase transition (Poirier, 1982; Brearley et al., 1992; Kirby et al., 1996) and of pyroxene to garnet (Hogrefe et al., 1994) have been studied for harzburgitic mantle composition so far. However, kinetic data of other phase transformations in the transition zone are necessary to allow for consistent treatment of kinetic effects on seismic properties within and above the transition zone.

The reaction rate constant k_0 has a minor effect on the seismic properties of the kinetically inhibited phase assemblage (Figure 11c). P- and S-wave velocity vary by ±0.05 km/s, and density is changed by ±0.02 g cm^{-3} for varying k_0 to its lower and upper bounds. The thickness of the low-velocity layer above the 660 km discontinuity shifts by ±4 km.

4.2 Seismological and geodynamic implications

Patterns of mantle flow and dynamics have been investigated using seismic wave speed anomalies in seismic tomography models (e.g., Li et al., 2008; Ritsema et al., 2011) and seismic waves sampling the upper mantle and mantle transition zone discontinuities using receiver functions (e.g., Vinnik, 1977; Farra & Vinnik, 2000; Rondenay, 2009), short period P'P' reflections (e.g., Niazi & Anderson, 1965; Vidale & Benz, 1993; Day & Deuss, 2013), and PP and SS precursors (e.g., Shearer, 1991; Deuss, 2009). Since the upper mantle and mantle transition zone discontinuities are sensitive to thermal variations due to their Clapeyron slopes (Bina & Helffrich, 1994; Helffrich, 2000; Weidner & Wang, 2000), variations of discontinuity depth and of transition zone thickness (i.e., the depth between the 410 and 660 km discontinuity) and constraints from mineral physics, are frequently used to infer thermal variations in the mantle (e.g., Shearer, 2000, Ritsema et al. 2009).

The investigation of reaction kinetics of the reaction from ferropericlase and bridgmanite to ringwoodite can add further constraints on mantle temperature and flow patterns. The effect of kinetic inhibition can be compared to seismic data using a two-step approach. In a first step, through forward modelling of synthetic seismograms for a range of temperatures, upwelling rates, and grain sizes. Relevant temperatures can be determined from adiabatic mantle geotherms (Brown & Shankland, 1981; Spiliopoulos, 1984; Ita & Stixrude, 1992; Cobden et al., 2008) to estimate excess temperatures (e.g., Sleep, 1990; Schilling, 1991; Herzberg et al., 2007). Heat flux estimates (e.g., Sleep, 1990; Courtillot et al., 2003) can be converted into

558 estimates for upwelling rates using convection models for vertical upwellings. A steady-state
559 axisymmetric plume with temperature-dependent viscosity might serve as a starting point for
560 estimates of upwelling rates as a function of heat flux and excess temperatures (Loper & Stacey,
561 1983; Schubert et al., 2001). In a second step, the seismic recordings can be compared to the
562 set of synthetic seismograms and those models are taken which give the best match with regard
563 to frequency dependent travel time residuals and amplitude ratios. The set of matching models
564 gives the range of corresponding grain sizes and upwelling rates.
565
566 Considering the effects of reaction kinetics of ferropericlase and bridgmanite to ringwoodite on
567 the amplitudes and travel times may offer additional constraints on mapping mantle flow using
568 P-to-s receiver functions. P-to-s conversions typically have higher frequencies (Li et al., 2000;
569 Wölbern et al., 2006). Several studies (van der Meijde et al., 2003; Schmandt, 2012; Huckfeldt
570 et al., 2013) show frequency dependent behaviour of P-to-s conversions at mantle transition
571 zone discontinuities. We see little frequency dependence of P-to-s conversion in our synthetic
572 models within the range typically used for receiver functions, but observe strong waveform
573 variations that are likely to be observable in recorded data as well as strong amplitude variations
574 and small travel time variations that might add additional constraints for detecting regions with
575 mantle upstreams.
576
577 The analysis of PP and SS precursors might have some resolution limitations with respect to
578 the scale of the mantle upwellings which might hamper the detection of the predicted
579 waveforms. Geodynamic modelling indicates that deep thermal mantle plumes have typical
580 diameters of ~200 km (e.g., Sleep, 1990; Schubert et al., 2001; Steinberger & Antretter, 2006)
581 whereas thermochemical plumes might have larger diameters ranging from 600 to 800 km
582 (Farnetani, 2005; Farnetani & Hofmann, 2010; Stockmann et al., 2019). Lessing et al. (2015)
583 use the 2.5-D axisymmetric finite difference technique PSVaxi (Jahnke, 2008; Thorne et al.,
584 2013) to examine the effects of topography of the upper mantle discontinuities imaged by PP
585 underside reflections with dominant periods of 2 s. Their models show that the PP wavefield
586 reflected off a locally elevated 660 km with a diameter of 200 to 400 km does not differ
587 significantly from the PP wavefield reflected off a flat reflector at 660 km depth. The size of
588 the detailed topography of the perturbed reflector is smaller than the PP Fresnel zone at 660 km
589 depth and thus might not be resolved. The detection of effects of the kinetically inhibited
590 reaction from ferropericlase and bridgmanite to ringwoodite might therefore be challenging in
591 narrow mantle upwellings. Although conduction might lead to thermal halos around narrow
592 mantle plumes the effect might be small (Sleep, 2004) and might not influence the detectability

of the plume using underside reflection. Nonetheless, recent tomographic images show that plumes might be broad upstreams (French and Romanowicz, 2015), very different to early numerical and laboratory plume experiments which might make the upstream detectable seismically. The pooling of plume material beneath the 660 km discontinuity due to the endothermic phase transition might lead to larger scale temperature anomalies in the region of plume-like mantle upstreams (Tackley et al., 1994, Schubert et al, 1995, Stockmann et al., 2019).Possible candidates for upwellings with large, detectable lateral dimensions are large transient domes near the mantle transition zone (Courtillot et al., 2003, Davaille et al., 2005, Kumagai et al., 2007; Kumagai et al., 2008). The transient domes are characterised by upwelling rates slower than deep mantle plumes due to their small buoyancy ratio (ratio of chemically driven buoyancy to thermally driven buoyancy). Nonetheless, the transient domes could have excess temperatures up to 300 K in their centre and form a thermal boundary layer with the ambient mantle (Davaille et al., 2005). Upwelling mantle material might pond beneath the 660 km discontinuity when encountering the phase transformation from bridgmanite and ferropericlase to ringwoodite (e.g., Schubert & Turcotte, 1975; Schubert & Tackley, 1995; Tackley, 1995; Steinbach & Yuen, 1997; Brunet & Yuen, 2000; Davaille et al., 2005, Farnetani & Samuel, 2005). Due to the negative Clapeyron slope, the transformation pressure of the warmer material is shifted towards lower pressure, resulting in a negative buoyancy force which delays further upwelling. The material starts to pond beneath the phase transformation (Davaille et al., 2005) and spreads laterally, growing with dimensions broader than plume conduits (e.g., Steinbach & Yuen, 1997; Davaille et al., 2005, Stockmann et al., 2019).

Furthermore, the viscosity contrast across the 660 km discontinuity (e.g., Mitrovica & Forte, 2004) might support lateral mantle flow beneath the discontinuity. The geodynamic models of Tosi & Yuen (2013) show additional evidence for horizontal flow whose scale is governed by the viscosity contrast due to temperature variations. For small values of the viscosity contrast, broad and highly viscous plumes are generated that tend to pass through the transition zone relatively unperturbed. For higher values of the viscosity contrast ($10^2 \leq \Delta\eta_T \leq 10^3$), the geodynamic simulations show horizontal channel flows beneath the 660 km discontinuity which might extend up to 1500 km horizontally before tilting to more vertical flow. Therefore, lateral mantle flow could change the fine-scale seismic structure at ~660 km depth in a way that could allow for the detection of the effects of kinetically inhibited growth with seismic methods sensitive to upper mantle discontinuity structure.

This study has predicted effects of kinetically inhibited growth of ringwoodite in mantle

upstreams and the expected effect on seismic probes for discontinuity structure. We find that the effect on PP/SS underside reflection travel times is small; amplitudes, although harder to assess in recorded data, might show a larger response to the altered discontinuity structure. For P-to-s conversions travel time effects are minor but waveforms and amplitudes of conversions are noticeably affected. Potentially P-to-s receiver function could be a suitable probe to detect kinetic effects in the phase transitions and to map out mantle flow.

5 Conclusions

The effects of reaction kinetics of bridgmanite and ferropericlase to ringwoodite in upwelling mantle on elastic properties were investigated using data of kinetic experiments and internally self-consistent thermodynamic modelling. As the kinetic experiments show, growth of ringwoodite is initiated at ferropericlase grain boundaries and is kinetically inhibited due to the necessary diffusion of chemical components. At the initiation of ringwoodite growth, bridgmanite transforms into metastable garnet. Ringwoodite grows from the metastable assemblage of ferropericlase and pyrope-bearing garnet.

The results of the analysis of kinetically inhibited transformation at ~660 km depth predict possible effects of kinetically inhibited growth of ringwoodite on seismic data which can be summarized as follows:

1. The increased amount of ferropericlase and garnet results in a localized low velocity zone of Δv_P ~ -5%, Δv_S ~ -7% directly above the 660 km seismic discontinuity due to the lower seismic velocities and density of ferropericlase and garnet compared to ringwoodite and bridgmanite. The impedance contrasts for P and S waves are thus increased compared with seismic velocity profiles of an equilibrated pyrolite mineral assemblage.
2. The effects of reaction kinetics on the seismic fine structure at ~660 km depth depend on the product of the squared grain size and upwelling rate. The change of seismic properties correlates with the product of squared grain size and upwelling rate. Modelling 1-D synthetic seismograms using the seismic profiles of kinetically inhibited phase assemblages show travel time delays of 0.4-0.8 s for PP precursors and delays of 1.2-1.6 s for SS precursors for kinetic inhibition of the ringwoodite-forming reaction. The finite width of the low-velocity layer above the seismic discontinuity results in frequency dependent behaviour of PP and SS underside reflection amplitudes, with higher amplitudes for 1-3 s PP waves and 5-8 s SS waves. However, high-frequency PP

and SS waves are rarely observed, and the predicted travel time differences are of similar magnitude as typical picking uncertainties. Hence, it might be challenging to utilize PP and SS underside reflections in order to observe kinetic effects.

3. Synthetic seismograms for P-to-s converted waves for velocity models for kinetically inhibited transformations predict strong waveform variations for higher temperature models and amplitude variations dependent on temperature, grain size and upwelling rate. Travel time variations are maximum ±0.3 s relative to models at equilibrium for temperature of 1960 K. Receiver functions therefore might be a suitable seismic probe to look for kinetic effects on the seismic structure of the 660 km discontinuity in mantle upwellings. A future re-evaluation of P-to-s receiver functions at mantle upwellings would be necessary to study the predicted effects described in this paper.
4. Possible candidates for mantle upwellings where reaction kinetics may become important are transient domes with low buoyancy ratios and large lateral dimensions, or broader scale plume upwellings. Material stalling at the phase transformation of bridgmanite and ferropericlase to ringwoodite might generate structure in the resolution range of P-to-s converted waves.

Data Availability

The resulting data of this work and sources code developed during this work are not publicly available. Except the results from kinetic experiments by Dobson & Mariani (2014), data are based on tools available in the public domain:

1. Perple_X program package (Connolly, 2005), utilising the elastic and thermodynamic properties and the solid solution model of Stixrude & Lithgow-Bertelloni (2011)
2. 1-D synthetic seismic modelling using the reflectivity method (Fuchs & Müller, 1971)
3. and data processing with seismic waveform analysis tool SeismicHandler (Stammler, 1993).

If you are interested in detailed data, please contact the corresponding author.

Acknowledgements

We are grateful for the constructive reviews by the editor Ian Bastow and two anonymous reviewers that helped to greatly improve the quality of the manuscript. We thank Jamie Connolly for assistance with the Perple_X program package (Connolly, 2005). Data analyses were carried out with SeismicHandler (Stammler, 1993). Figures were produced with Generic

Mapping Tools (GMT) (Wessel & Smith, 1995). S. Lessing was supported under grant DFG TH1530/2–1. The high-pressure kinetic experiments were largely performed at the Bayerisches Geoinstitut under the aegis of an EU large-scale facility grant to D. Rubie and an Alexander von Humboldt fellowship to D. Dobson. The Al- free experiment was performed at the ETH Zurich during a visiting professorship by D. Dobson. We acknowledge funding from NERC (grants NE/L006898 and NE/L007363). L. Cobden was supported under grant DFG TH1530/5–1.

References

Allègre, C. J. & Turcotte, D. L., 1986, Implications of a two-component marble-cake mantle. Nature, 323(6084), 123-127.

Brearley, A. J., Rubie, D. C. & Ito, E., 1992, Mechanisms of the transformations between the α, β and γ polymorphs of Mg2SiO4 at 15 GPa. Physics and Chemistry of Minerals, 18(6), 343-358.

Brunet, D. & Yuen, D. A., 2000, Mantle plumes pinched in the transition zone, Earth Planet. Sci. Lett., 178, 13-27.

Brown, J. M. & Shankland, T. J., 1981. Thermodynamic parameters in the Earth as determined from seismic profiles, Geophys. J. R. Astron. Soc., 66, 579-596.

Cobden, L., Goes, S., Cammarano, F. & Connolly, J. A. D., 2008, Thermochemical interpretation of one-dimensional seismic reference models of the upper mantle: evidence for bias due to heterogeneity, Geophys. J. Int., 175, 627-648.

Cobden, L. & Thomas, C., 2013, The origin of D ″reflections: a systematic study of seismic array data sets. Geophys. J. Int., 194(2), 1091-1118.

Connolly, J. A. D., 1990, Multivariable phase-diagrams-an algorithm based on generalized thermodynamics, American Journal of Science, 290, 666-718.

Connolly, J. A. D., 2005, Computation of phase equilibria by linear programming: a tool for geodynamic modeling and its application to subduction zone decarbonation, Earth Planet. Sci. Lett., 236, 524-541.

Courtillot, V., Davaille, A., Besse, J. & Stock, J., 2003, Three distinct types of hotspots in the Earth's mantle, Earth Planet. Sci. Lett., 205 (3-4), 295-308.

Crotwell, H. P., Owens, T. J. & Ritsema, J., 1999, The TauP toolkit: Flexible seismic travel-time and ray-path utilities, Seism. Res. Lett., 70, 154-160.

Cserepes, L. & Yuen, D.A., 2000, On the possibility of a second kind of mantle plume, Earth Planet. Sci. Lett., 183, 61–71.

Davaille, A., 1999, Simultaneous generation of hotspots and super-swells by convection in a heterogeneous planetary mantle, Nature, 402, 756–760.

Davaille, A., Stutzmann, E., Silveira, G., Besse, J. & Courtillot, V., 2005, Convective patterns under the Indo-Atlantic box, Earth Planet. Sci. Lett., 239, 233–252.

Davies, D., Kelly, E. & Filson, J., 1971, Vespa process for analysis of seismic signals Nature-Physical science, 232, 8-13.

Day, E. A. & Deuss, A., 2013, Reconciling PP and P'P' precursor observations of a complex 660 km discontinuity, Geophys. J. Int., doi: 10.1093/gji/ggt122.

Deuss, A., 2009, Global Observations of Mantle Discontinuities Using SS and PP Precursors, Surv. Geophys., 30, 301-326.

744 Dobson, D. P., Mariani, E., 2014, The kinetics of the reaction of majorite plus ferropericlase to
745 ringwoodite: Implications for mantle upwellings crossing the 660 km discontinuity, Earth
746 Planet. Sci. Lett., 408, 110-118.
747 Durand, S., Chambat, F., Matas, J. & Ricard, Y., 2012, Constraining the kinetics of mantle
748 phase changes with seismic data. Geophys. J. Int., 189(3), 1557-1564.
749 Dziewonski, A. M. & Anderson, D. L., 1981, Preliminary Reference Earth Model, Phys. Earth
750 Planet. Inter., 25, 297-356.
751 Farber, D. L., Williams, Q. & Ryerson, F. J., 1994, Diffusion in Mg2SiO4 polymorphs and
752 chemical heterogeneity in the mantle transition zone. Nature, 371(6499), 693-695.
753 Farnetani, C. G. & Samuel, H., 2005, Beyond the thermal plume paradigm, Geophys. Res. Lett.,
754 32, doi:10.1029/2005GL022360.
755 Farnetani, C.G. & Hofmann, A. W., 2010, Dynamics and internal structure of the Hawaiian
756 plume, Earth Planet. Sci. Letters, 295, 231 – 240.
757 Faul, U. H. & Jackson, I., 2005, The seismological signature of temperature and grain size
758 variations in the upper mantle. Earth Planet. Sci. Lett., 234(1), 119-134.
759 Fei, H., Faul, U. & Katsura, T., 2021. The grain growth kinetics of bridgmanite at the topmost
760 lower mantle, Earth Planet. Sci. Lett., 561, 116820.
761 French, S. W. & Romanowicz, B. (2015). Broad plumes rooted at the base of the Earth's
762 mantle beneath major hotspots. Nature, 525(7567), 95–99.
763 Fuchs, K. & Müller, G., 1971, Computation of synthetic seismograms with the reflectivity
764 method and comparison with observations, Geophys. J. R. Astr. Soc., 23, 417-433.
765 Fukao, Y. & Widiyantoro, S., Obayashi, M., 2001, Stagnant slabs in the upper and lower mantle
766 transition region, Rev. Geophys., 39, 291-323.
767 Fukao, Y., Obayashi, M. & Nakakuki, T., Deep Slab Project, 2009. Stagnant slab: a review.
768 Ann. Rev. Earth Planet. Sci. 37, 19-46.
769 Gasparik, 1996a, Diopside-jadeite join at 16-22 GPa, Phys. Chem. Mineral., 23, 476-486.
770 Gasparik, 1996b, Melting experiments on the enstatite-diopside join at 70-224 kbar, including
771 the melting of diopside, Contrib. Mineral. Petrol., 124, 139-153.
772 Green, D. H. & Ringwood, A. E., 1967, The genesis of basaltic magmas, Contributions to
773 Mineralogy and Petrology, 15, 103-190.
774 Guo, Z., Zhou, Y, 2020, Finite-frequency imaging of the global 410-and 660-km discontinuities
775 using SS precursors, Geophys. J. Int., 220(3), 1978-1994.Helffrich, G. R., 2000,
776 Topography of the transition zone seismic discontinuities, Rev. Geophys., 38, 141-158.
777 Herzberg, C., Asimov, P. D., Arndt, N., Niu, Y., Lesher, C. M., Fitton, J.G., Cheadle, M. J. &
778 Saunders, A. D., 2007, Temperatures in ambient mantle and plumes: constraints from
779 basalts, picrites, and komatiites, Geochem. Geophys. Geosys., 8,
780 doi:10.1029/2006GC001390.
781 Hill, R., 1965, Continuum micro-mechanics of elastoplastic polycrystals, J. Mech. Phys. Solids
782 ,13, 89-101.
783 Hirose, K., 2002, Phase transitions in pyrolitic mantle around 670-km depth: Implications for
784 upwelling of plumes form the lower mantle, J. Geophys. Res.-Solid Earth, 107(B4), 2078.
785 Hofmann, A. W. & Hart, S. R. (1978). An assessment of local and regional isotopic equilibrium
786 in the mantle. Earth Planet. Sci. Lett., 38(1), 44-62.
787 Hogrefe, A., Rubie, D. C., Sharp, T. G. & Seifert, F., 1994, Metastability of enstatite in deep
788 subducting lithosphere, Nature, 372, 351 – 353, doi:10.1038/372351a0
789 Huckfeldt, M., Courtier, A.M. & Leahy, G.M., 2013. Implications for the origin of Hawaiian
790 volcanism from a converted wave analysis of the mantle transition zone. Earth Planet.
791 Sci. Lett., 373, 194-204.
792 Irifune, T., Nishiyama, N., Kuroda, K., Inoue, T., Isshiki, M., Utsumi, W., Funakoshi, K.,
793 Urakawa, S., Uchida, T., Katsura, T. & Ohtaka, O., 1998, The postspinel phase boundary
794 in Mg_2SiO_4 determined by in situ X-ray diffraction, Science, 279, 1698-1700, DOI:
795 10.1126/science.279.5357.1698.

Ita, J. & Stixrude, L., 1992, Petrology, elasticity and composition of the mantle transition zone, J. Geophys. Res.-Solid Earth, 97(B5), 6849-6866.
Jackson, I., 2007. Properties of rocks and minerals—physical origins of anelasticity and attenuation in rock. Treatise on geophysics, 2, 493-525.
Jahnke, G., 2008, Methods for seismic wave propagation on local and global scales with finite differences, PhD thesis, Ludwig Maximilians-Universität München.
Kennett, B. L. N., Engdahl, E. R.& Buhland, R., 1995, Constraints on seismic velocities in the Earth from travel-times, Geophys. J. Int., 122, 108-124.
Kellogg, J. B., Jacobsen, S. B. & O'Connell, R. J., 2002, Modeling the distribution of isotopic ratios in geochemical reservoirs. Earth Planet. Sci. Lett., 204(1), 183-202.
Kirby, S. H., Stein, S., Okal, E. A. & Rubie, D. C., 1996, Metastable mantle phase transformations and deep earthquakes in subducting oceanic lithosphere, Rev. Geophys., 34, 261-306.
Korenaga, J., 2005. Firm mantle plumes and the nature of the core–mantle boundary region. Earth Planet. Sci. Let., 232, 29-37.
Kubo, T., Ohtani, E., Kato, T., Urakawa, S., Suzuki, A., Kanbe, Y., Funakoshi, K., Utsumi, W., Kikegawa, T. & Fujino, K., 2002, Mechanisms and kinetics of the post-spinel transformation in Mg_2SiO_4, Phys. Earth Planet. Inter., 129, 153-171.
Kubo, T., Ohtani, E., Kato, T., Kondo, T., Hosoya, T., Sano, A. & Kikegawa, T., 2008, Kinetics of the post-garnet transformation: Implications for density and rheology of subducting slabs, Phys.- Earth Planet. Inter., 170, 181-192.
Kumagai, I., Davaille, A. & Kurita, K., 2007, On the fate of thermally buoyant mantle plumes at density interfaces, Earth Planet. Sci. Lett. 254, 180-193.
Kumagai, I, Davaille, A., Kurita, K. & Stutzmann, E., 2008, Mantle plumes: Thin, fat, successful, or failing? Constraints to explain hot spot volcanism through time and space, Geophys. Res. Lett., 35, L16301, doi:10.1029/2008GL035079.
Langrand, C., Andrault, D., Durand, S., Konôpková, Z., Hilairet, N., Thomas, C. & Merkel, S., 2019, Kinetics and detectability of the bridgmanite to post-perovskite transformation in the Earth's D ″layer. *Nature communications*, *10*(1), 1-9.
Lessing, S., Thomas, C., Rost, S., Cobden, L. & Dobson, D.P., 2014, Mantle transition zone structure beneath India and Western China from migration of PP and SS precursors. Geophy. J. int. Doi: 10.1093/gji/ggt511.
Lessing, S., Thomas, C., Saki, M., Schmerr, N.C. & Vanacore, E., 2015, On difficulties of detecting PP Precursors, Geophys. J. Int., *201*(3), 1666-1681.
Li, X., Kind, R., Priestley, K., Sobolev, S. V., Tilmann, F., Yuan, X., & Weber, M., 2000, Mapping the Hawaiian plume conduit with converted seismic waves, Nature, 405(6789), 938 – 941.
Li, C., van der Hilst, R., Meltzer, A. S. & Engdahl, E. R., 2008, Subduction of the Indian lithosphere beneath the Tibetan Plateau and Burma, Earth Planet. Sci. Lett., 274, 157-168.
Li, L. & Weidner, D. J. (2008). Effect of phase transitions on compressional-wave velocities in the Earth's mantle. Nature, 454(7207), 984-986.
Loper, D. E. & Stacey, F. D., 1983, The dynamical and thermal structure of deep mantle plumes, Earth Planet. Sci. Lett., 33, 304-317.
Mitrovica, J. & Forte, A. M., 2004, A new inference of mantle viscosity based upon joint inversion of convection and glacial isostatic adjustment data, Earth Planet. Sci. Lett., 225, 177–189.
Montagner, J.P. & Kennett, B. L. N., 1995, How to reconcile body-wave and normal-mode reference Earth models?, Geophys. J. Int., 125, 229-248.
Müller, G., 1985, The reflectivity method: a tutorial, Jour. Geophys., 58, 153-174.
Muirhead, K. & Datt, R., 1976, N-th root process applied to seismic array data, Geophysical Journal of the Royal Astronomical Society, 47(1), 197-210.

Negi, S. S., Kumar, A., Ningthoujam, L. S. & Pandey, D. K. (2022). Mapping the mantle transition zone beneath the Indian Ocean geoid low from Ps receiver functions. Tectonophysics, 831, 229330. https://doi.org/10.1016/J.TECTO.2022.229330
Poirier, J. P., 1981, On the kinetics of olivine-spinel transition, Physics of the Earth and Planetary Interiors, 26(3), 179-187.
Putnis, A. (1992). An introduction to mineral sciences. Cambridge University Press.
Reuss, A., 1929, Berechnung der Fließgrenze von Mischkristallen auf Grund der Konstanten des Einkristalls, Z. Angew. Math. Mech., 9, 49.
Ricard, Y., Matas, J. & Chambat, F., 2009. Seismic attenuation in a phase change coexistence loop, Phys. Earth Planet. Inter., 176, doi:10.1016/j.pepi.2009.04.007.
Richards, P.G., 1972, Seismic waves reflected from velocity gradient anomalies within the Earth‘s upper mantle, Z. Geophys., 38, 517-527.
Ringwood, A. E., 1969, Phase transformations in the Mantle, Earth Planet. Sci. Lett., 5, 401.
Ritsema, J., Xu, W., Lithgow-Bertelloni, C. & Stixrude, L., 2009, Estimates of the transition zone temperature in a mechanically mixed upper mantle, Earth Planet. Sci. Lett., 277, 244–252.
Ritsema, J., Deuss, A., van Heijst, H. J. & Woodhouse, J. H., 2011, S40RTS: a degree-40 shear-velocity model for the mantle from new Rayleigh wave dispersion, teleseismic travel time and normal-mode splitting function measurements, Geophys. J. Int., 184, 3, 1223-1236.
Rost, S. & Weber, M., 2002, The upper mantle transition zone discontinuities in the Pacific as determined by short-period data, Earth Planet. Sci. Lett., 204, 347-361.
Rost, S. & Thomas, C., 2002, Array Seismology: Methods and Applications, Rev. Geophys., 40, 2-1 - 2-27.
Saikia, A., Frost, D. J. & Rubie, D. C., 2008. Splitting of the 520-kilometer seismic discontinuity and chemical heterogeneity in the mantle, Science, 319, 1515-1518.
Saki, M, Thomas, C., Nippress, S. & Lessing, S., 2014, Topography of upper mantle seismic discontinuities beneath the North Atlantic: the Azores, Canary and Cape Verde plumes, Earth Planet. Sci. Lett., in preparation.
Schilling, J-G., 1991, Fluxes and excess temperatures of mantle plumes inferred from their interaction with migrating mid-ocean ridges, Nature, 352, 397-403.
Schmandt, B., 2012, Mantle transition zone shear velocity gradients beneath USArray, Earth Planet. Sci. Lett., 355-356, 119-130.
Schmerr, N. & Thomas, C., 2011, Subducted lithosphere beneath the Kuriles from migration of PP precursors, Earth Planet. Sci. Lett., 311, 101-111.
Schubert, G., Yuen, D.A. & Turcotte, D. L., 1975, Role of phase transitions in a dynamic mantle, Geophys. J. R. Astron. Soc., 42, 705–735.
Schubert, G., Anderson, C., & Goldman, P. (1995). Mantle plume interaction with an endothermic phase change. J. Geophys. Res.-Solid Earth, 100(B5), 8245–8256.
Schubert, G. & Tackley, P. J., 1995, Mantle dynamics: The strong control of the spinel-perovskite transition at a depth of 660 km, J. Geodynamics, 20(4) 417-428,
Schubert, G., Turcotte, D. L. & Olson, P., 2001, Mantle convection in the Earth and Planets, Cambridge University Press.
Schweitzer, J., Fyen, J., Mykkeltveit, S., Gibbons, S. J., Pirli, M., Kühn, D. & Kvaerna, T., 2002, Seismic Arrays, IASPEI new manual of seismological observatory practice, 80pp.
Shearer, P. M., 1991, Constraints on Upper Mantle Discontinuities From Observations of Long-Period Reflected and Converted Phases, J. Geophys. Res.-Solid Earth, 96, 18147-18182.
Shearer, P. M., 2000, Earth’s Deep Interior: Mineral Physics and Tomography from the Atomic to the Global Scale, AGU, 115-131.
Shim, S. H., Duffy, T. S. & Shen, G., 2001, The post-spinel transformation in Mg_2SiO_4 and its relation to the 660-km seismic discontinuity, Nature, 411, 571-574.

898 Shimojuku, A., Boujibar, A., Yamazaki, D., Yoshino, T., Tomioka, N. & Xu, J., 2014, Growth
899 of ringwoodite reaction rims from MgSiO3 perovskite and periclase at 22.5 GPa and
900 1,800°C. Phys. Che. Minerals, 41, 555-567. DOI: 10.1007/s00269-014-0669-x.
901 Sleep, N. H., 1990, Hotspots and mantle plumes: Some phenomenology, J. Geophys. Res.-Solid
902 Earth, 95, 6715-6736.
903 Sleep, N. H.,2004. Thermal haloes around plume tails. Geophys. J. Int., 156(2), 359–362.
904 Solomatov, V.S., 1996. Can hotter mantle have a larger viscosity? Geophys. Res. Let. 23, 937-
905 940.
906 Solomatov, V.S., El-Khonzondar, R. & Tikare, V., 2002. Grain size in the lower mantle:
907 constrains from 510 numerical modeling of grain growth in two-phase systems. Phys.
908 Earth Planet. Inter., 129, 265–282.
909 Spiliopoulos, S., 1984. The earth's thermal profile - is there a mid-mantle thermal-boundary
910 layer?, J. Geodyn., 1, 61-77.
911 Stammler, K., 1993, Seismic Handler: programmable multichannel data handler for interactive
912 and automaticprocessing of seismological analysis, Computers and Geoscience, 19, 135-
913 140.
914 Steinbach, V. & Yuen, D. A., 1997, Dynamical effects of a temperature- and pressure-
915 dependent lower-mantle rheology on the interaction of upwellings with the transition
916 zone, Physics of the Earth and Planetary Interiors, 103, 85-100.
917 Stixrude, L. & Lithgow-Bertelloni, C., 2005. Thermodynamics of mantle minerals – I. Physical
918 properties, Geophys. J. Int., 162, 610-632.
919 Stixrude, L. & Lithgow-Bertelloni, C., 2011, Thermodynamics of mantle minerals—II. Phase
920 equilibria, Geophys. J. Int., 184, 1180-1213.
921 Sung, C.-M. & Burns, R. G., 1976, Kinetics of high-pressure phase transformations:
922 implications to the evolution of the olivine-spinel transition in the downgoing lithosphere
923 and its consequences on the dynamics of the mantle, Tectonophysics, 31, 1—32.
924 Tackley, P. J., 1995. On the penetration of an endothermic phase transition by upwellings and
925 downwellings, J. Geophys. Res.-Solid Earth, 100, 15477-15488.
926 Tackley, P. J., Stevenson, D. J., Glatzmaier, G. a. & Schubert, G. (1994). Effects of multiple
927 phase transitions in a three-dimensional spherical model of convection in Earth's mantle.
928 J. Geophys. Res.-Solid Earth, 99(B8), 15877–15901.
929 Tackley, P.J., Xie, S., Nakagawa, T. & Hernlund, J.W., 2005, Numerical and laboratory studies
930 of mantle convection: philosophy, accomplishments, and thermochemical structure and
931 evolution, in Earth's Deep Mantle: Structure, Composition and Evolution, 83-99, eds Van
932 der Hilst, R., Bass, J.D., Matas, J. & Trampert, J., American Geophysical Union,
933 Washington DC.
934 Tammann, G., 1920, Über Anlauffarben von Metallen, Z. Anorg. Allg. Chem., 111, 78.
935 Thomas, C. & Billen, M., 2009, Upper mantle structure along a profile in the southwest Pacific,
936 Geophys. J. Int., 176, 113-125.
937 Thompson, D., 2012, Seismic discontinuity structure beneath the Canadian Shield and the
938 signature of continental roots, PhD thesis, University of Bristol, Great Britain.
939 Thorne, M.S., Garnero, E.J., Jahnke, G., Igel, H. & McNamara, A.K., 2013, Mega ultra low
940 velocity zone and mantle flow, Earth Planet. Sci. Lett., 364, 59-67.
941 Tosi, N. & Yuen, D.A., 2011, Bent-shaped plumes and horizontal channel flow beneath the 660
942 km discontinuity, Earth Planet. Sci. Lett., 312, 348-359.
943 Trampert, J., Deschamps, F., Resovsky, J. & Yuen, D., 2004, Probabilistic tomography maps
944 chemical heterogeneities throughout the lower mantle, Science, 306, 853-856.
945 Vacher, P., Mocquet, A. & Sotin, C., 1998, Computation of seismic profiles from mineral
946 physics: the importance of the non-olivine components for explaining the 660 km depth
947 discontinuity, Phys. Earth Planet. Inter., 106, 275-298.
948 Vinnik, L., 1977, Detection of waves converted from P to SV in the mantle, Phys. Earth Planet.
949 Inter., 15, 39-45.

950 Voigt, W., 1928, Lehrbuch der Kristallphysik, Teubner, Berlin.
951 Wang, Y., Uchida, T., Zhang, J., Rivers, M. L. & Sutton, S. R., 2004. Thermal equation of state
952 of akimotoite $MgSiO_3$ and effects of the akimotoite-garnet transformation on seismic
953 structure near the 660 km discontinuity, Phys. Earth Planet. Inter., 143/144, 57–80.
954 Waszek, L., Tauzin, B., Schmerr, N.C., Ballmer, M.A. & Afonso, J.C., 2021, A poorly mixed
955 mantle transition zone and its thermal state inferred from seismic waves. Nat. Geosci. **14,**
956 949–955. https://doi.org/10.1038/s41561-021-00850-w
957 Watson, E. B. & Price, J. D., 2002, Kinetics of the reaction MgO+Al2O3→MgAl2O4 and Al-
958 Mg interdiffusion in spinel at 1200 to 2000 °C and 1.0 to 4.0 GPa. Geochim. Cosmochim.
959 Acta, 66, 2123-2138.
960 Weidner, D. J. & Wang, Y., 2000, Phase transformations: implications for mantle structure, in:
961 Earth's Deep Interior: Mineral Physics and Tomography from the Atomic to the Global
962 Scale, AGU, 117, 215-235.
963 Wessel, P. & Smith, W. H. F., 1995, New version of the Generic Mapping Tools released, Eos
964 Transactions AGU, 76, 329.
965 White, R. S. & McKenzie, D., 1995, Mantle plumes and flood basalts, J. Geophys. Res.-Solid
966 Earth, 100, 17543-17858.
967 Wölbern, I., Jacob, A.W.B., Blake, T.A., Kind, R., Li, X., Yuan, X., Duennebier, F. & Weber,
968 M., 2006. Deep origin of the Hawaiian tiltered plume conduit derived from receiver
969 functions. Geophys. J. Int. 166, 767–781.
970 Xu, F., Vidale, J., Earle, P., Benz, H., 1998, Mantle discontinuities under southern Africa from
971 precursors to P'P'df, Geophys. Res. Lett., 25, 571-574.
972 Yamazaki, D., Kato, T., Ohtani, E. & Toriumi, M., 1996. Grain growth rates of MgSiO3-
973 perovskite and periclase under lowermantle conditions. Science 274, 2052–2054.
974 Yamazaki, D., Inoue, T., Okamoto, M. & Irifune, T. (2005). Grain growth kinetics of
975 ringwoodite and its implication for rheology of the subducting slab. Earth Planet. Sci.
976 Lett., 236(3), 871-881.
977
978

Figures

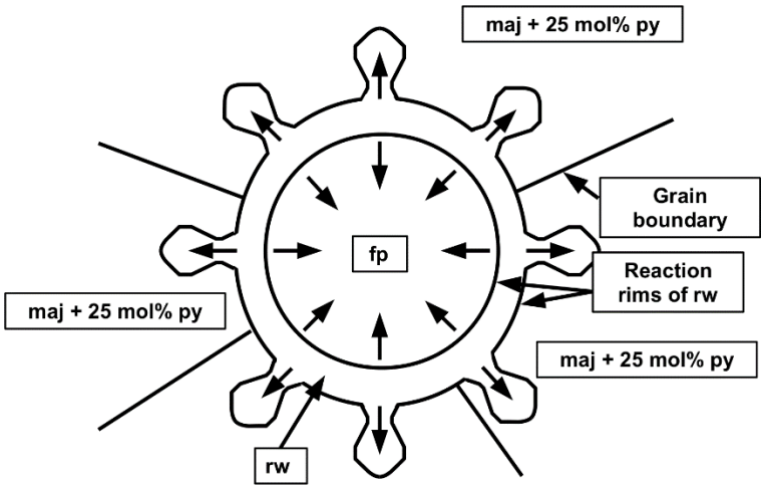

Figure 1: Sketch of the reaction mechanism for the recombination of bridgmanite and ferropericlase (fp) to ringwoodite (rw). The ringwoodite layer nucleates on the fp grain surface and grows into majorite garnet (maj) which contains 25 mol% Al-bearing pyrope (py) in a fingering instability. After Dobson & Mariani (2014).

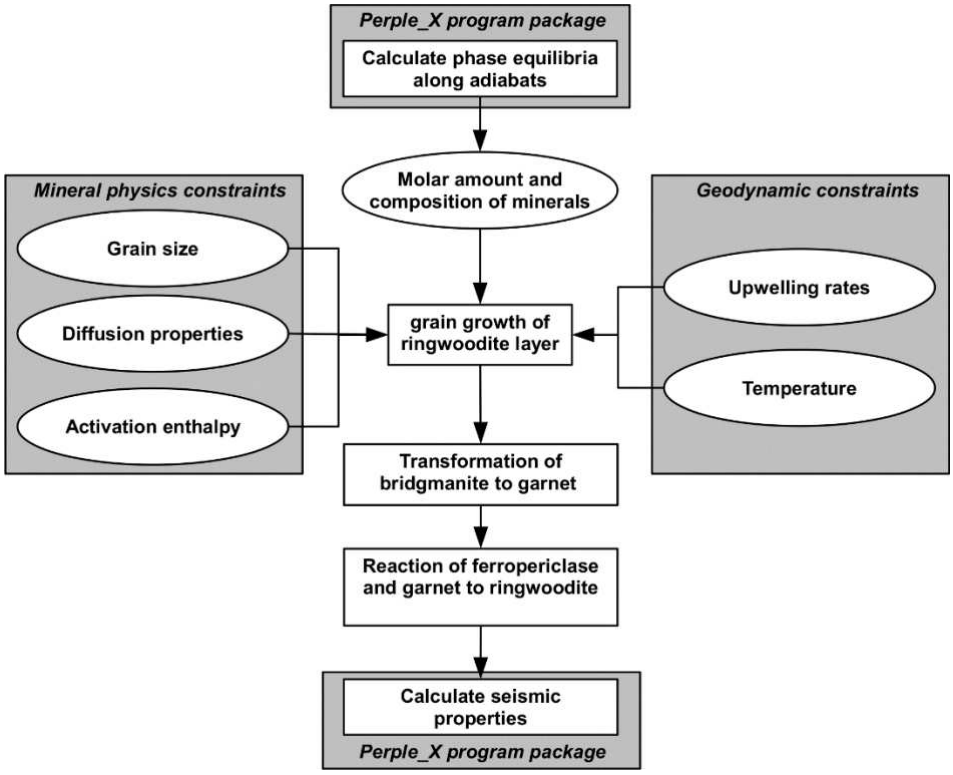

Figure 2: Forward modelling of seismic properties for kinetically inhibited growth of ringwoodite and corresponding mineral reactions for ferropericlase, bridgmanite and garnet.

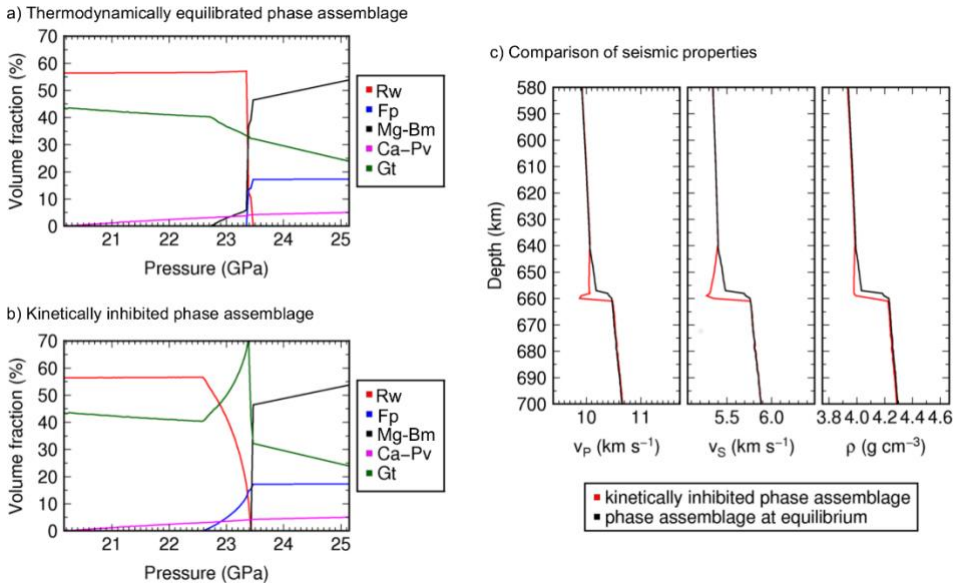

993
994

995 **Figure 3:** Example for effects of kinetic inhibition of ringwoodite growth on volume fractions
996 of minerals and on seismic properties of phase assemblages for temperature of 1850 K
997 (following the 1300°C adiabat), 5 cm initial grain size and 50 cm/yr upwelling rate. a) Volume
998 fractions of equilibrated phase assemblages as a function of pressure for pyrolite composition
999 along the 1300°C adiabat. Mineral phases are abbreviated as follows: Rw: ringwoodite, Fp:
1000 ferropericlase, Mg-Bm: magnesium bridgmanite, Ca-Pv: calcium perovskite, Gt: garnet. b)
1001 Volume fractions of kinetically inhibited phase assemblages as a function of pressure for
1002 pyrolite composition along the 1300°C adiabat. c) Comparison of seismic velocities and density
1003 between equilibrated and kinetically inhibited phase assemblages.
1004

d

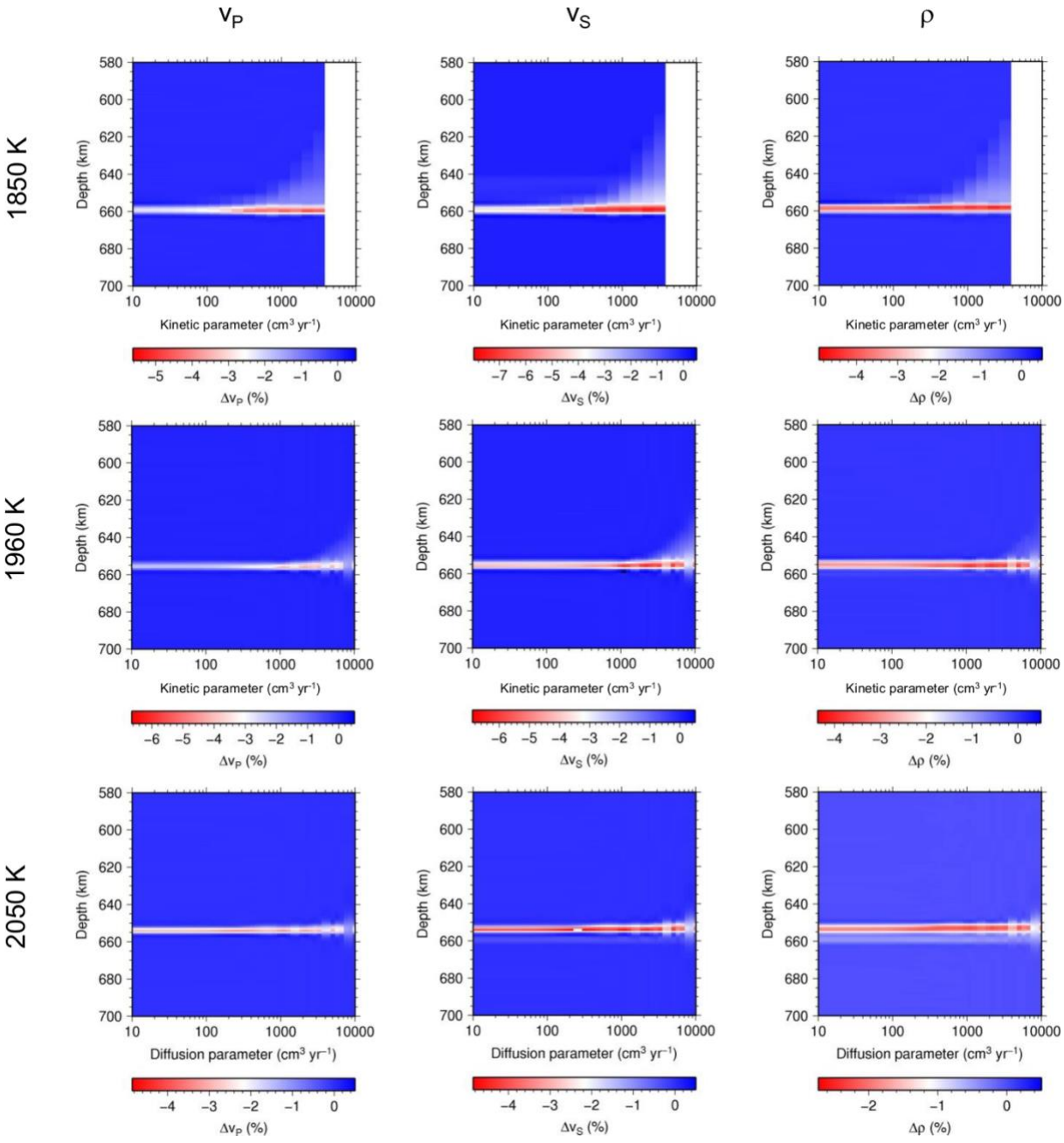

Figure 4: Relative differences of P wave velocity, S wave velocity and density due to the kinetically inhibited growth of ringwoodite and the presence of metastable ferropericlase and garnet for temperatures of 1850 K, 1960 K and 2050 K. No data are available for kinetic parameters > 4000 $cm^3\ yr^{-1}$ because the ringwoodite growth interferes with the ringwoodite-to-wadsleyite transition. To date, no studies with kinetic data for the ringwoodite-to-wadsleyite transition in mantle upstreams are known to the authors.

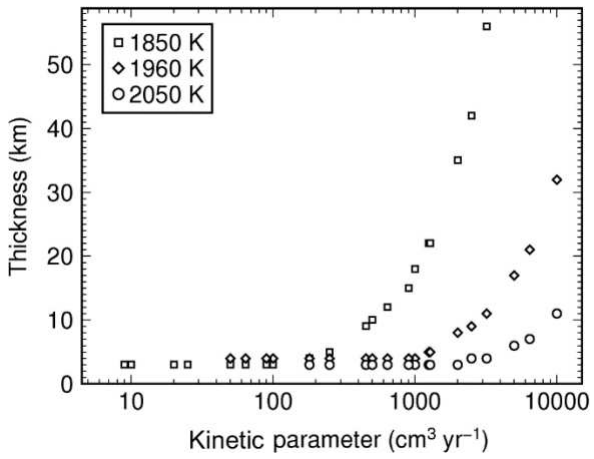

Figure 5: Thickness of the reaction interval where ringwoodite grows from the recombination of ferropericlase and garnet as function of the kinetic parameter D. The kinetic parameter D is proportional to the upwelling rate v and the square of grain size d, for simplicity we set the proportion factor to unity so that $D = v\ d^2$. Scenarios which have different grain size and upwelling rates, but have the same kinetic parameter, show the same kinetic inhibition.

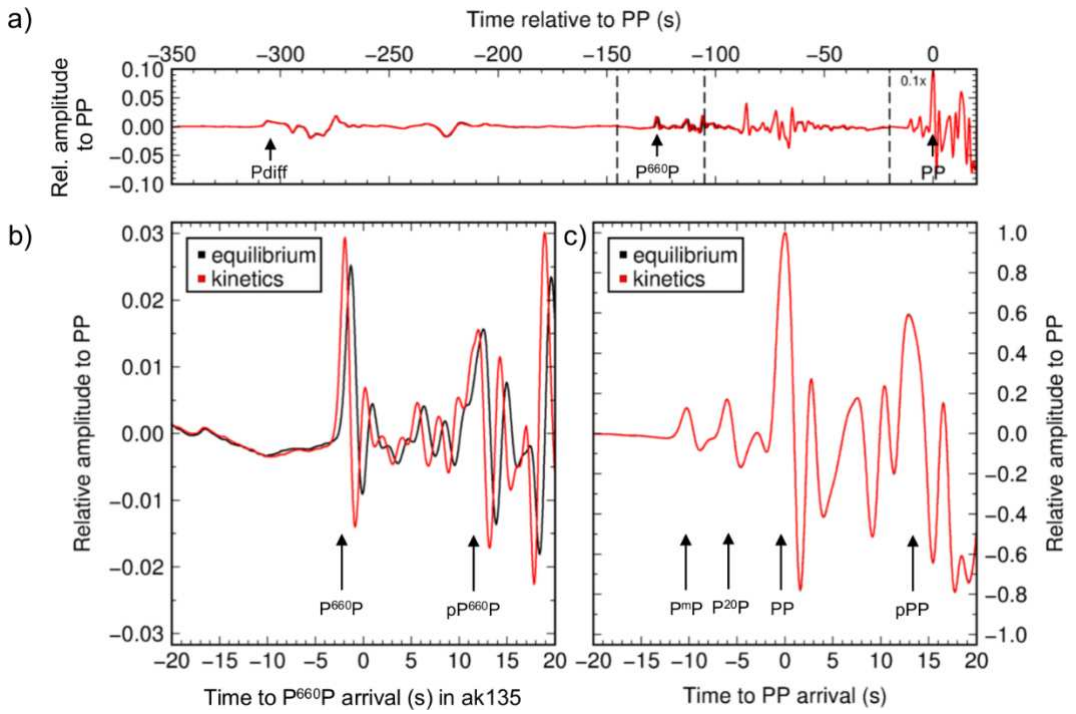

Figure 6: Synthetic seismograms of PP precursors with a dominant period of 3 s from seismic models of equilibrated and kinetically inhibited phase assemblages at an array with reference epicentral distance of 120 deg, a temperature of 1850 K, grain size of 5 cm and a vertical upwelling rate of 50 cm/yr. a) shows the linearly stacked traces of all calculated seismograms for equilibrated pyrolite phase assemblages (black) and kinetically inhibited phase assemblages (red) aligned with slowness for PP from ak135 (Kennett et al., 1995). Time windows around the predicted arrivals of P660P and PP from ak135 shown b) and c) and are marked by vertical lines and the phase names. Arrows indicate the arrivals of P660P and pP660P in zoomed diagram b) and the arrivals of PP and pPP in zoomed diagram c).

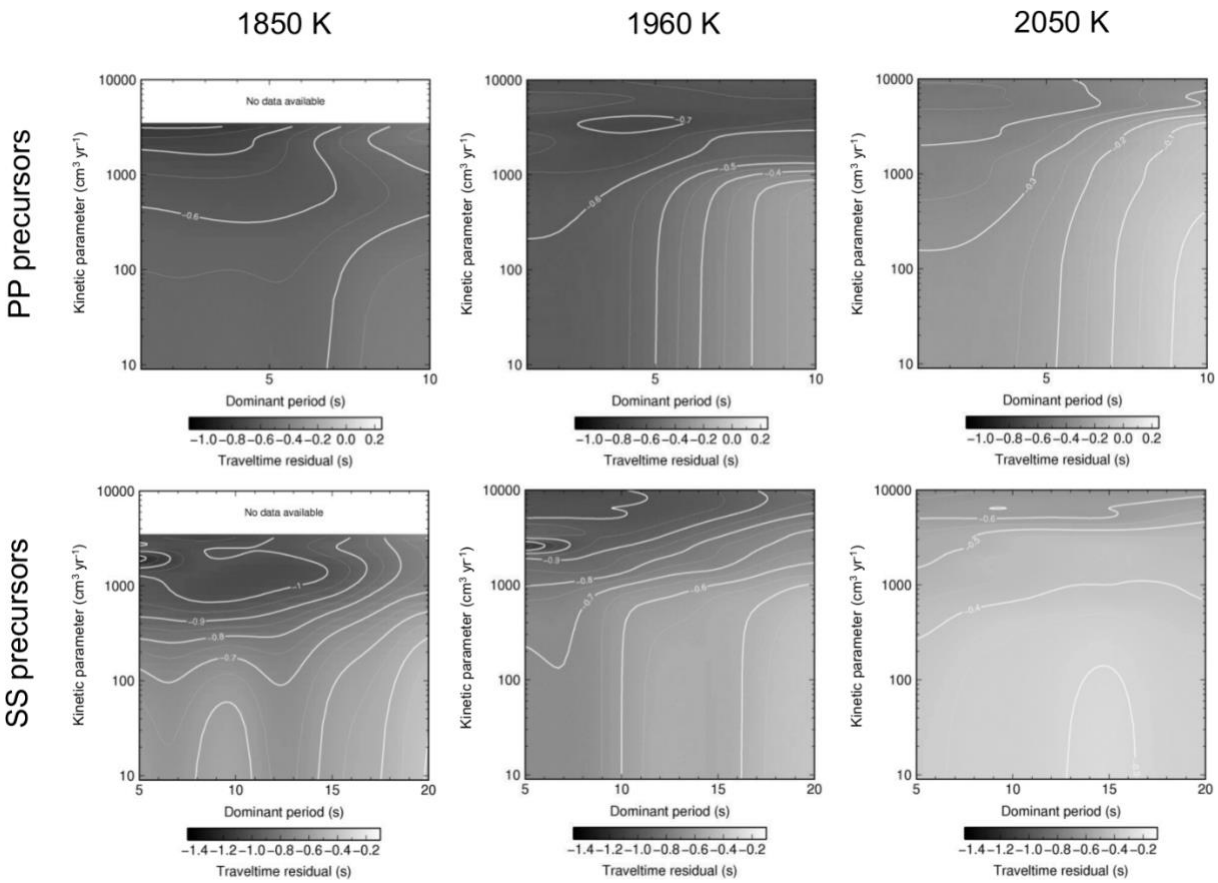

Figure 7: Travel time residuals of stacked PP and SS precursors between kinetically inhibited and equilibrated backward reaction to ringwoodite as a function of temperature and kinetic parameter for varying dominant periods at an epicentral distance of 120°C. Bold lines denote changes of travel time residuals by 0.1, thin lines denotes changes of travel time residuals by 0.05. Data are not available at temperature pf 1850 K and kinetic parameters > 4000 cm^3 yr^{-1} (cf. Figure 4).

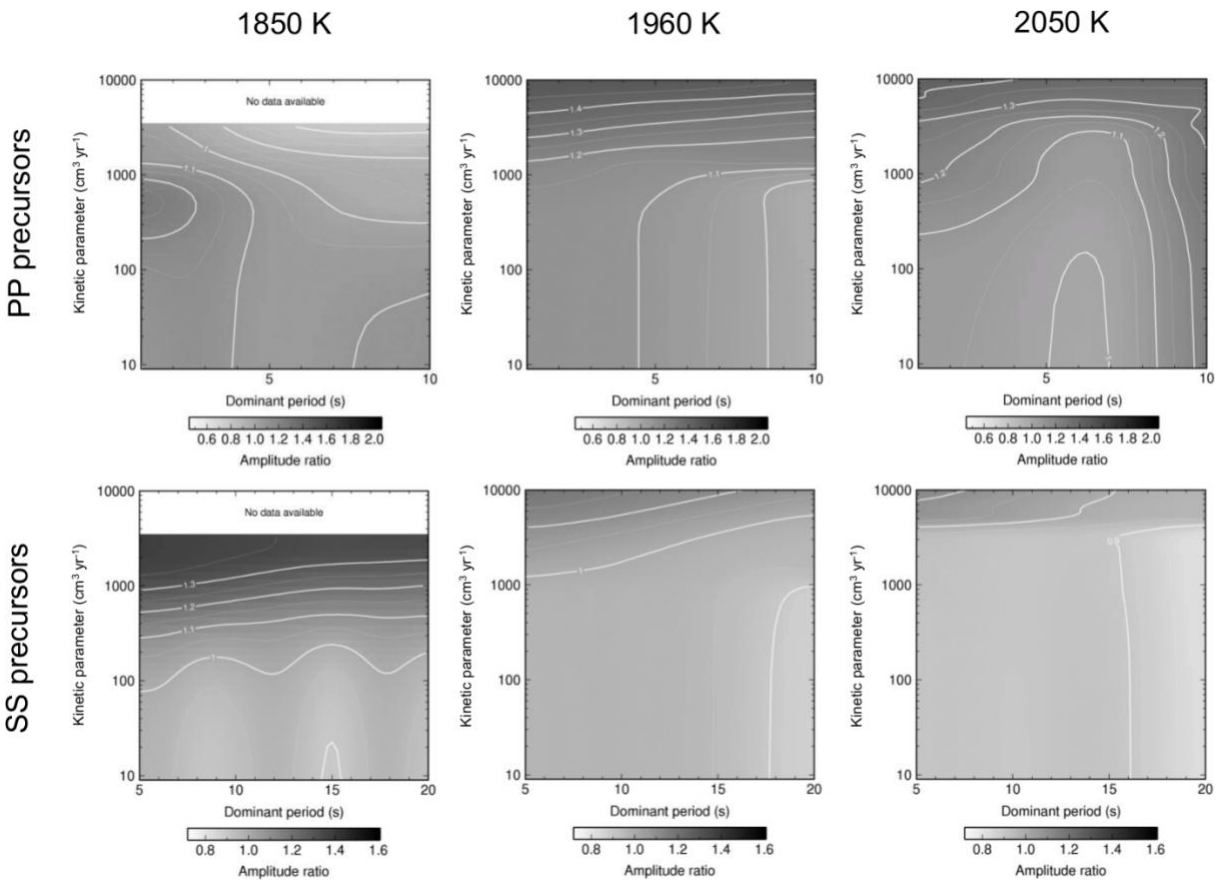

Figure 8: PP and SS precursor amplitude ratios of reflections off the kinetically inhibited reaction vs. off the equilibrated reaction to ringwoodite as a function of temperature and kinetic parameter for varying dominant periods at an epicentral distance of 120°. Bold lines denote changes of amplitude ratios by 0.1, thin lines denote changes of amplitude ratios by 0.05. Data are not available at temperature pf 1850 K and kinetic parameters > 4000 cm^3 yr^{-1} (cf. Figure 4).

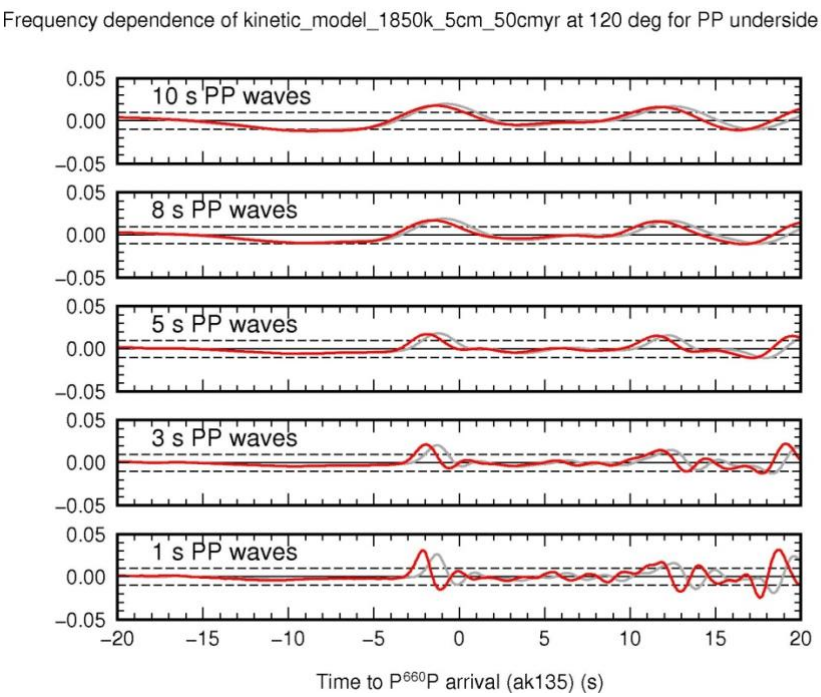

Figure 9: Frequency dependence of $P^{660}P$ underside reflections for equilibrated and kinetically inhibited phase assemblages at 1850 K, for 5 cm grain size and 50 cm/yr upwelling rate for dominant periods of 1 to 10 s. Waveforms of reflections off the kinetically inhibited backward reaction to ringwoodite are depicted in red, whereas waveforms of reflections off the equilibrated backward reaction to ringwoodite are depicted in black.

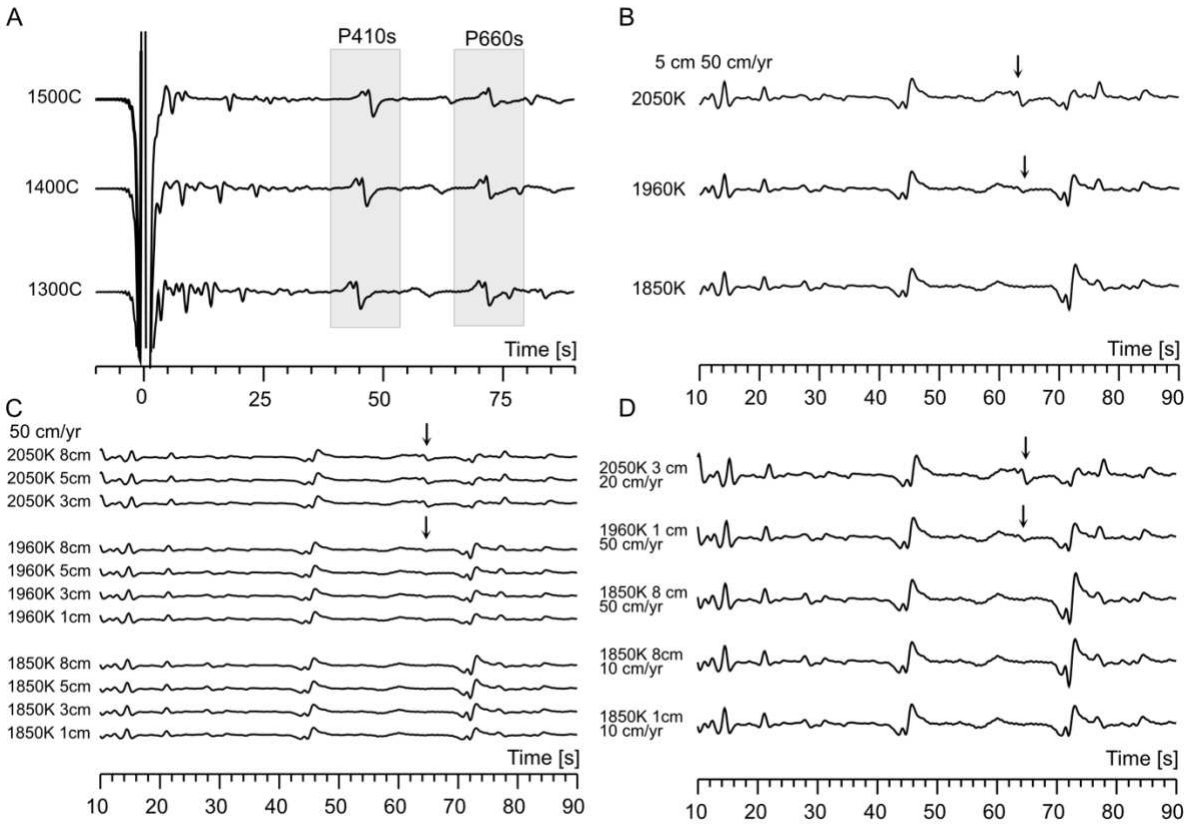

Figure 10: Synthetic waveforms for P-to-S conversions arriving in the P-wave coda with dominant period of 1 s. All traces are recorded at 43 deg epicentral distance and aligned on the theoretical P-wave arrival. All times are given relative to P-wave arrival time. A) Waveforms for pyrolytic models at equilibrium conditions for mantle adiabats with surface potential temperatures ranging from 1300 to 1500 °C. P-to-s conversions from the 410-km discontinuity and the 660 km discontinuity are highlighted. B) Waveforms for kinetically inhibited transformation for models with 5 cm grain sizes and an upwelling rate of 50 cm/yr for geotherms at 1850 K, 1960 K and 2050 K. Amplitudes are normalized on the P-wave amplitude. Arrows indicate detectable precursors to P660s. C) Waveforms for kinetically inhibited transformation for 50 cm/yr upwelling rate and varying temperatures and grain sizes. Amplitudes are normalized on the P-wave amplitude. Arrows indicate detectable precursors to P600s. D) Waveforms for kinetically inhibited transformation for varying temperatures, upwelling rates and grain sizes. Amplitudes have not been normalized and the amplitude variations of the P-to-S conversion from the ferropericlase and bridgmanite to ringwoodite are observable. Arrows indicate detectable precursors to P660s.

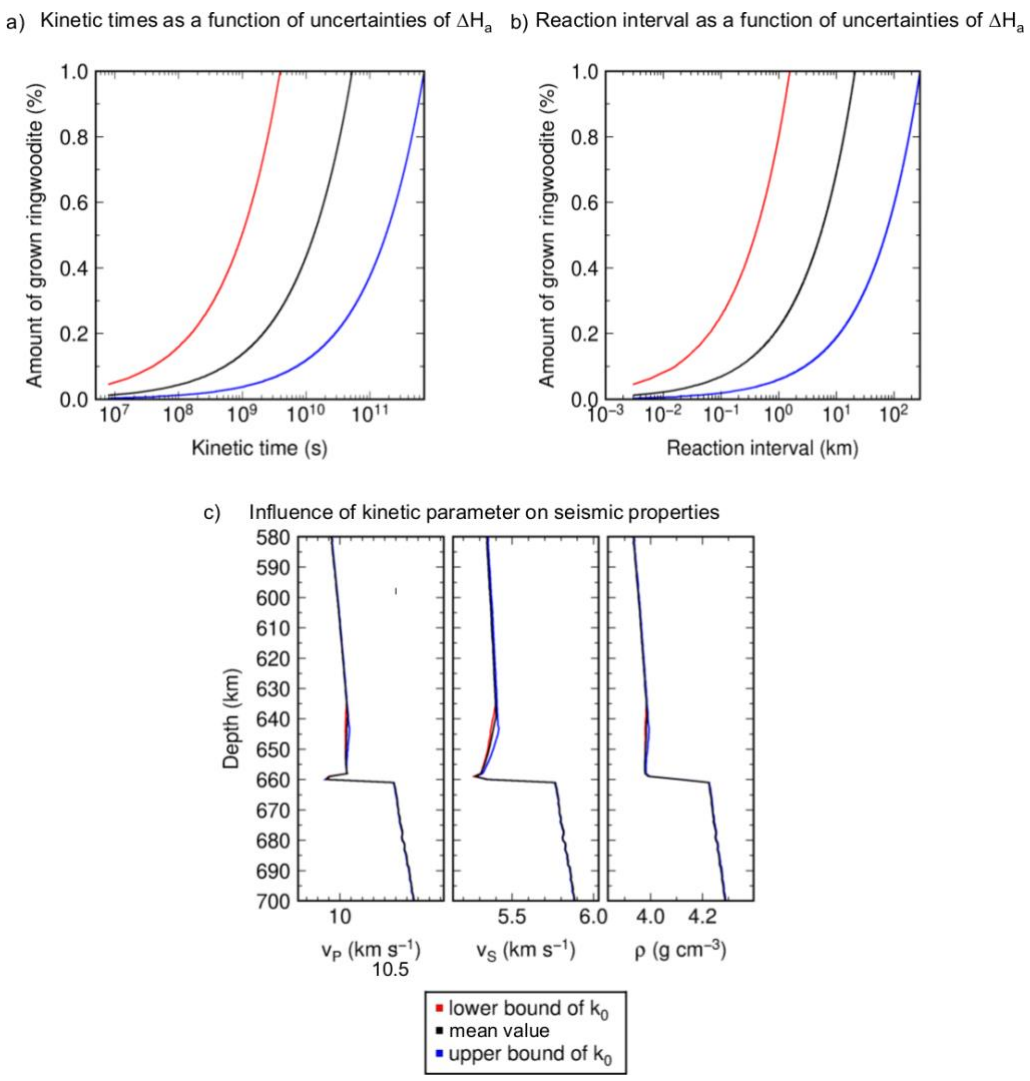

Figure 11: Effects of uncertainties of kinetic parameters on seismic properties of kinetically inhibited phase assemblages and thickness of the low-velocity layer above the onset of ringwoodite growth. The effects have been calculated for an ambient mantle temperature of 1850 K, an initial grain size of 5 cm and an upwelling rate of 50 cm/yr. a) Effects of uncertainties of the enthalpy ΔH_a on the growth time of ringwoodite. The red curve denotes the calculation for the lower bound of ΔH_a from Table 3 whereas the blue curve the upper bound of ΔH_a. b) Effects of uncertainties of the enthalpy ΔH_a on the width of inhibited ringwoodite. c) Effects of uncertainties of the diffusion coefficient k_0 on the seismic wave speeds and density. The lower and upper bound of k_0 correspond to the uncertainties in Table 3.

Tables:

Table 1: Pyrolite composition by Sun et al. (1982) used in this study. The oxides of the CFMAS system are given as molar percentages.

SiO_2	MgO	Al_2O_3	FeO	CaO
38.61	49.13	2.77	6.24	3.25

Table 2: Relationship between surface potential temperature of a mantle adiabat and their ambient temperatures at ~23.4 GPa, i.e., at ~660 km depth. Surface potential temperature are often given in °C (e.g., Cammarano et al., 2005; Cobden et al., 2008) whereas ambient temperatures are usually given in K.

Potential temperature (°C)	1300	1400	1500
Ambient temperature (K)	1850	1960	2050

Table 3: Parameter range for calculating the seismic properties of kinetically inhibited phase assemblages.

Parameter	Value(s)
From the kinetic experiments by Dobson & Mariani (2014):	
Enthalpy of the reaction ΔH_a (kJ mol^{-1})	456±40
Diffusion coefficient ln(k_0) (m^2/s)	-6.36±0.25
For modelling seismic properties:	
Temperatures (K)	1850, 1960, 2050
Grain size (cm)	1, 5, 10, 20
Upwelling rate (cm/yr)	1, 5, 10, 50, 100